A first step towards Quantum Computing in Rare-earth-ion-doped crystals

Master's thesis
by
Tomas Christiansson

Lund Reports on Atomic Physics, LRAP-266
Lund, Februari 2001

Abstract

This master's thesis explores the fascinating area of quantum computing. A new promising technique using rare-earth-ion-doped inorganic crystals at cryogenic temperatures is investigated. This paper gives a brief introduction to the subject and reports on the first experimental work on this concept.

The first step towards realising this quantum computing concept has successfully been demonstrated: The initial preparation steps for the construction of the quantum computers most fundamental part, the qubit.

Contents

Chapter 1

Introduction

Today's computers are rapidly becoming faster and smaller. According to *Moore's law* the performance of the microprocessor doubles every 18 months. If the progress continues, each transistor will consist of not more than a few atoms by the year 2020. When the logic gates consist of just a few atoms, quantum mechanics will come to play an important part. It will set the limit for the performance of today's technology.

The concept of quantum mechanics in computing offers new and exciting prospects. The *Quantum Turing Machine* was first described by *David Deutsch* [1]. His ideas have been further developed by numerous scientists, see [2] for a survey of the quantum computing history.

For a more thorough description of quantum computing see [2] or [3]. The book by *William* and *Clearwater* [4] offers a popular survey of quantum computing.

1.1 Theory of quantum computing

The concepts that make quantum computing feasible are the principles of superposition and entanglement.

Quantum superposition is one of the fundamental properties of every quantum system. A system, Ψ, can thus be in a *coherent superposition* of two (or more) states

$$\Psi = a\Psi_a + b\Psi_b. \tag{1.1}$$

It is not until one makes a measurement on the system that its state becomes well-defined. The probability for finding the system in state Ψ_a is $|a|^2$ and for Ψ_b it is $|b|^2$.

A very important aspect of this superposition is the *quantum coherence*. This means that the phase, φ, is well-defined:

$$\Psi = |a|\,\Psi_a + |b|\,e^{i\varphi}\Psi_b. \tag{1.2}$$

The essential point of this coherence is that there exist a basis where the state becomes well-defined. In an incoherent mixture of the states no such basis exists.

Consider the quantum system Ψ' to be in an even coherent superposition of the two states Ψ_a and Ψ_b with $\varphi = 0°$.

$$\Psi' = 1/\sqrt{2}\,(\Psi_a + \Psi_b)\,. \tag{1.3}$$

If a *Hadamard transformation*,

$$H\Psi_a \rightarrow 1/\sqrt{2}\,(\Psi_a + \Psi_b) \text{ and} \tag{1.4}$$

$$H\Psi_b \rightarrow 1/\sqrt{2}\,(\Psi_a - \Psi_b)\,, \tag{1.5}$$

is applied to the system the state becomes

$$H\Psi' = \Psi_a. \tag{1.6}$$

The Hadamard transformation will in general give results depending on the value of φ.

Besides quantum computing *quantum entanglement* offers thrilling concepts of *quantum teleportation*[5]. Entanglement can exist between two or more particles or quantities. For instance, the polarisation states of two different photons can be entangled. It is possible to create a two photon system where one of them is horizontally polarised and the other is vertically polarised,

$$\frac{1}{\sqrt{2}}\,(|H>_1\,|V>_2 + |V>_1\,|H>_2) \tag{1.7}$$

but where it is not clear which one of them has the horizontal polarisation. It is not until the time of measurement that the states of the two photons become well-defined. If the measurement is made on one of the photons, the state of the other collapses simultaneously. This leads to the famous *EPR*-paradox [6].

Entanglement and superposition forms the foundations on which quantum computing is being built. Without them the quantum computer would be no different than an ordinary classical computer.

The quantum computer schemes that are being implemented today are a kind of *Quantum Registry Machines* which uses quantum two-level systems as qubits. A qubit is the quantum equivalent of the classical bit. The quantum logic gates are usually implemented through some sort of external manipulations of the qubits such as lasers directed at individual atoms.

There are of course difficulties involved in the design of a quantum computer. The main problem is that the quantum systems must be isolated from the environment.

Each quantum logic gate performed on the qubits will cause noise in the system. The noise level introduced by every operation performed on the quantum computer makes it difficult to implement. The discovery of *Quantum Error Correction* [7] has shown that one can reduce the noise, using imperfect corrections, in the system without collapsing its superposition.

1.2 Quantum versus classical computation

The first *Quantum Turing Machine* was presented as early as 1985 [1]. At that time it was not clear if there were any practical applications of such a machine. It was not easy to find algorithms where the quantum equivalent was significantly better than the classical counterpart.

The breakthrough came when *Shor* [8] in 1994 presented an algorithm for factoring large integers. For sufficiently large integers this task is intractable on a classical computer since the number of computations scales super-polynomially with the size of the integer. *Shor* discovered that on a quantum computer this would only scale cubically.

After this first useful algorithm was discovered the quantum computer field became a very hot topic and research has started all over the world. The quantum computer concept that has got the most media coverage is the *NMR* technique described below.

1.3 Quantum computing concepts

There have been many proposals for quantum computer concepts including Nuclear Magnetic Resonance (NMR), Ion traps, High-Q optical cavities, Quantum dots and Buckminster-Fullerenes. The two concepts where most work has been done are NMR and Ion traps.

1.3.1 Nuclear Magnetic Resonance

The NMR concept is derived from the well known NMR-technique. Special molecules are chosen to work as quantum computer and different parts act as different qubits. The two levels of the qubit are the different nuclear spin states of, e.g., hydrogen atoms in the molecule. The resonance energies of the transitions between these nuclear spin states are a little different depending on the chemical environment around the hydrogen atoms. It is therefore possible to address different qubits using different frequencies of the RF-field.

NMR-quantum computers have been built with up to 7 qubits, but there still remains some controversy. It is not clear if NMR can serve as a true quantum computer since the system cannot be prepared in a pure state, i.e. with all the atoms in the same state, when the computation starts.

1.3.2 Ion traps

The concept of using laser cooled ions trapped in linear ion traps is another promising technique. A linear string of ions is placed inside a high-vacuum chamber. A laser beam can be directed at each individual ion and the interaction between ions is caused by phonon vibrations in the string.

Chapter 2

Rare-earth-ion quantum computers

If rare-earth-ions are doped into inorganic crystals they will, at liquid helium temperatures, show very long homogeneous dephasing (quantum coherence) times. As a long quantum coherence time is a prerequisite for making a quantum computer, that is not very easily fulfilled in solid state materials, this is a good reason to carefully look into the possibility of using these rare-earth materials as quantum computer hardware.

Another condition, which normally is difficult to fulfil, is that there must be a way of making each qubit interact with the other qubits. In these crystals the individual rare-earth-ions will have typical line widths in the kHz region while the inhomogeneous broadening of an ensemble of ions can be in the GHz region. If you wish to make one qubit consist of ions at frequency ν_0 and another qubit at $\nu_1 = \nu_0 + \Delta\nu$ they must be made to interact in some way independent of the value of $\Delta\nu$. If this is possible one has come a long way in the making of a small quantum computer.

To get such an interaction one can make use of the fact that the ions have a difference in permanent dipole moment between the excited state and the ground state. If one of the ions is put into the excited state it will shift the absorption frequencies of the other ions.

A possibly suitable ion to use here is Eu^{3+} doped into $YAlO_3$ or Y_2SiO_5. The crystal used in the following experiments is the latter. The lifetime in its hyperfine levels is many hours and the energy separations between the hyperfine levels are tens of MHz. It turns out that this makes it easy to learn how to construct the qubit.

2.1 Theory

As a theoretical tool for the further discussion I will briefly go through the *Bloch vector* formalism, for a more detailed description see [9] and [10]. To begin, I start with a quick survey of quantum mechanics fundamentals using the *Dirac notation.*

2.1.1 Quantum mechanics survey

Any quantum system can be described by the *Schrödinger equation*

$$\hat{H}|\Psi>= i\hbar\frac{d|\Psi>}{dt}, \tag{2.1}$$

where $\hat{H}$ is the Hamiltonian.

A quantum state can in general be expanded in any set of basis wave functions, ϕ_i. These basis wave functions are generally chosen to be eigenfunctions of a chosen operator $\hat{A}$. Such a set of basis wave functions fulfils the equation

$$<\phi_i|\phi_j>= \delta_{ij}, \tag{2.2}$$

where δ_{ij}, the *Kronecker delta*, is equal to 1 if $i = j$ and 0 otherwise.

The operator $\hat{A}$ can thus be written as a diagonal matrix

$$\hat{A}|\phi_j> = a_j|\phi_j> \Rightarrow <\phi_i|\hat{A}|\phi_j>= a_j <\phi_i|\phi_j> = a_j\delta_{ij}. \tag{2.3}$$

The wave function can be expanded in terms of spatial and temporal parts.

$$\Psi(\vec{r},t) = \sum c_n(t)u_n(\vec{r}), \tag{2.4}$$

where $u_n(\vec{r})$ are the Hamiltonians basis wave functions.

Since the *Schrödinger equation* governs the temporal evolution of the quantum system we can omit the spatial part of the wavefunction. From now on I will use the following description of the quantum state.

$$|\Psi>= \begin{bmatrix} c_0(t) \\ c_1(t) \\ \vdots \\ c_{n-1}(t) \end{bmatrix} \tag{2.5}$$

Where the $c_i(t)$s are the time evolutions of the corresponding eigenstates. As we mainly will be concerned with two level systems we use the *two-level approximation*, therefore $n = 2$.

The expectation value of an operator is given by

$$<\hat{A}>=<\Psi|\hat{A}|\Psi>=<\sum_i c_i(t)|\hat{A}|\sum_j c_j(t)>= \sum_{i,j} c_i(t)^* c_j(t)A_{ij}. \tag{2.6}$$

With regard to this equation we introduce the *density matrix*

$$\rho_{ij} = c_i(t)^* c_j(t) = |\Psi><\Psi|. \tag{2.7}$$

In more general terms Equation 2.7 is expanded to be an ensemble average (over many atoms). To mark this a bar is put over the c_is.

$$\rho_{ij} = \overline{c_i(t)^* c_j(t)} = |\Psi><\Psi|. \tag{2.8}$$

The diagonal elements of the density matrix are the classical probabilities of finding an atom in the corresponding state.

The time evolution of the *density matrix* is given by

$$\frac{d\rho_{ij}}{dt} = c_i^* \frac{dc_j}{dt} + c_j \frac{dc_i^*}{dt}. \tag{2.9}$$

If we now look at the *Schrödinger equation*, Equation 2.1, again we see that it can be written as

$$\frac{dc_j}{dt} = \frac{-i}{\hbar} \sum_k c_k H_{jk} \tag{2.10}$$

and for c_i^* it becomes

$$\left(\frac{dc_i}{dt}\right)^* = \frac{i}{\hbar} \sum_k c_k^* H_{ik}^* = \frac{i}{\hbar} \sum_k c_k^* H_{ki}. \tag{2.11}$$

Putting these two equations into the time evolution of the density matrix gives

$$\frac{d\rho_{ij}}{dt} = \frac{-ic_i^*}{\hbar} \sum_k c_k H_{jk} + \frac{ic_j}{\hbar} \sum_k c_i H_{ki} = \frac{i}{\hbar} \sum_k (\rho_{kj} H_{jk} - H_{ki} \rho_{ik}) = \frac{i}{\hbar} \left[\hat{\rho}, \hat{H}\right] i. \tag{2.12}$$

This is the so-called *Liouville equation.*

2.1.2 Bloch equations

Let us now assume that there are only two levels involved in our systems, the ground and the excited state. The *density matrix* will then only have four components.

The energy difference between the two states is

$$\omega_{eg} = \frac{E_e - E_g}{\hbar}. \tag{2.13}$$

Considering only dipole interactions between the two levels we have a dipole operator given by

$$\mu = \begin{bmatrix} 0 & \mu_{ge} \\ \mu_{eg} & 0 \end{bmatrix}. \tag{2.14}$$

We introduce the *Rabi frequency*

$$\Omega = \frac{-\mu \cdot \mathbf{E}(\vec{r}, t)}{\hbar} \tag{2.15}$$

where $\mathbf{E}$ is the electro-magnetic field, and the frequency detuning

$$\Delta = \omega - \omega_{eg}, \tag{2.16}$$

where ω is the frequency of the electro-magnetic field.

Using the following kind of transformation of the off-diagonal matrix elements

$$\tilde{\rho}_{ge} = e^{-i\omega t}\rho_{ge}, \tag{2.17}$$

one can now show [10] that the *Liouville equation* can be written as

$$\frac{d\tilde{\rho}}{dt} = -\frac{i}{\hbar}\left[\hat{H}_{eff}, \tilde{\rho}\right]. \tag{2.18}$$

in the *rotating wave approximation* (the field oscillation is much faster than any other frequency in the system). The effective Hamiltonian is then written as

$$\hat{H}_{eff} = \begin{bmatrix} \hbar\Delta & \hbar\Omega \\ \hbar\Omega & 0 \end{bmatrix}. \tag{2.19}$$

By the following variable substitutions $w = \tilde{\rho}_{ee} - \tilde{\rho}_{gg}$, $u = \tilde{\rho}_{ge} + \tilde{\rho}_{eg}$ and $v = i\left(\tilde{\rho}_{ge} - \tilde{\rho}_{eg}\right)$, it is possible to deduce the *Bloch equations* from Equation 2.18. They are

$$\dot{u} = -\Delta v - \Gamma_2 u \tag{2.20}$$

$$\dot{v} = \Delta u - 2\Omega w - \Gamma_2 v \tag{2.21}$$

$$\dot{w} = 2\Omega v - \Gamma_1(w - w_0) \tag{2.22}$$

where $\Gamma_1 = 1/T_1$ and $\Gamma_2 = 1/T_2$. The two relaxation times are the upper state lifetime, T_1, and the homogeneous dephasing time, T_2. The initial population is given by w_0, if its value is -1 the initial population is in the ground state.

2.1.3 Bloch vector formalism

One way of illustrating the *Bloch equations* is by describing them using a vector in the (u, v, w)-space. We regard the values of u, v and w as the different components of a vector, the *Bloch vector*, in this space. The *Bloch equations* governs the motion of this vector in the *Bloch vector diagram.*

If one neglects the effects of relaxation processes the length of the *Bloch vector*, $\mathbf{R}(u, v, w)$, is equal to 1. It is then confined to what is called the *Bloch sphere* since the vector will always move on a sphere with radius 1.

The vector $\mathbf{R}$'s projection on the w-axis tells us where the population is. If $\mathbf{R}$ is aligned straight down along the w-axis all the atoms are in the ground state,

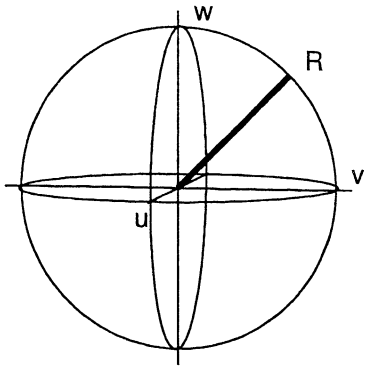

Figure 2.1: Bloch vector diagram

if it points upwards all the atoms are in the excited state. As long as the *Bloch vector* moves on the *Bloch sphere* all the atoms will be in a superposition of the two states. If the value of the w-component is zero the system is in an equal superposition of the two states.

The u- and v-axis are related to the phase coherence of the two states relative to the phase of the electro-magnetic field, i.e. the off-diagonal terms of the *density matrix*, as can be seen from the definitions of u and v in Equations 2.20 and 2.21. The u component is the part of the system that is in phase with the electro-magnetic field and the v component is the part that is out of phase.

The two relaxation constants causes the *Bloch vector* to move in the diagram. The factor Γ_1 causes the vector to relax in the $-w$-direction towards its initial value, w_0. The other relaxation constant, Γ_2, correspond to the loss of coherence in the system. It forces the u and v components towards zero, this also causes the vector to decrease in length.

When an external electro-magnetic field is applied the vector will start to move in the diagram. When the *Bloch vector* is moving the usual way of describing its movement is in the *frame* of the electro-magnetic field. In this case the movement along the u and v axis correspond to a relative change of the systems phase, i.e. the relative phase of the two quantum states, to the phase of the electro-magnetic field.

If we at first assume that there is no frequency detuning in the system, i.e. $\Delta = 0$, and that the relaxation can be neglected the u-component will not change in time and we can therefore let it be zero. When the field is applied both the v and w components will start to increase. The *Bloch vector* starts to rotate counter clockwise in the (v, w)-plane, as seen in Figure 2.1 above.

If the frequency detuning is not zero ($\Delta \neq 0$) the vector will also rotate around the w-axis since the time dependence of u and v are cross coupled. A full description is outside the scope of the present description, therefore see [11].

2.1.4 The π- and $\pi/2$-pulse

When an electromagetic field is applied to the system the *Bloch vector* will start to move. For a field tuned in resonance with the transition the *Bloch vector* moves on great circles through $w = -1$ and $w = 1$. If the field causes the *Bloch vector* to rotate 180° to its anti-parallel position it is called a π-pulse. This pulse can for instance move all the atoms from their ground states to their excited states.

Another pulse of interest is the $\pi/2$-pulse. It causes the *Bloch vector* to rotate 90° on the great circle. It can, for instance, transfer all the atoms from the ground state to an even superposition of the ground and excited states. For further information see [11].

2.2 Excitation-induced frequency shifts

Any quantum computing scheme requires a way of making the qubits interact. The method of our choice is excitation-induced frequency shifts. This has been thoroughly investigated in e.g. [12].

The key point is that the rare-earth-ions have different permanent electric dipole moments in their ground and excited states. The interaction between two ions can be described by

$$\nu = \nu_0 + D \tag{2.23}$$

where ν_0 is the original absorption frequency of the ion and D represents the induced shift.

$$D = \eta(0)\frac{(\delta\mu)^2}{4\pi\epsilon_0 h r^3} \tag{2.24}$$

where r is the distance between the neighbouring ions, h is *Plancks constant* and ϵ_0 is the permittivity of free space.

$$\eta(\nu) = \frac{1}{\epsilon(\nu)}\left(\frac{\epsilon(\nu)+2}{3}\right)^2 \tag{2.25}$$

where $\epsilon(\nu)$ is the dielectric constant at frequency ν.

The difference in permanent electric dipole moment ($\delta\mu = |\mu_e - \mu_g|$) in Eu^{3+} : Y_2SiO_5 at site 2 can be calculated by

$$\delta\mu = \frac{3h}{\epsilon(0)+2}\left|\frac{\Delta\nu_0}{E_{ext}}\right| \tag{2.26}$$

where the value of $|\Delta\nu_0/E_{ext}|$ is 17 kHz/(V cm^{-1}) [12]. The value of $\epsilon(0)$ is taken to be 11. There are currently no values given in the literature, but this value has been estimated using capacitance measurements on Y_2SiO_5 and $YAlO_3$.

The result of the frequency shift of two ions separated by 1 nm is $D \approx 15$ MHz and for 10 nm it is 15 kHz.

2.3 Quantum computing scheme

The rare-earth-ion-doped crystals contain a large number of frequency channels, i.e. the ratio between the inhomogeneous and the homogeneous line widths is large. One qubit can thus be chosen from ions that have an absorption frequency, ν_0, and other qubits are chosen from other parts of the inhomogeneous profile. For further information see [13].

The two-level system representing the qubit is chosen to be two of the ground state hyperfine levels. The remaining hyperfine level is used as a reservoir state. The definitions can be seen in Figure 2.2 and the energy separations are listed in Table 3.1 on page 22. When doing *Raman* transitions between the two qubit states an excited state is used, in order to make the discussion easier to understand only one of the three hyperfine states in the excited level is used.

Figure 2.2: Energy level diagram showing the states relevant for the quantum computing scheme including the two qubit states. The different labels in the picture corresponds to the atomic states as follows: $|e> \rightarrow {}^5D_0$, $|0> \rightarrow {}^7F_{0,\pm 1/2}$, $|1> \rightarrow {}^7F_{0,\pm 3/2}$ and $|a> \rightarrow {}^7F_{0,\pm 5/2}$. The last index in each label corresponds to the Eu^{3+}-ions nuclear spin projection on the symmetry axis of the ion in its site within the Y_2SiO_5 crystal.

Throughout this report I have assumed that the hyperfine levels are as described in Figure 2.2. However, it is not clear if the energy of the ${}^7F_{0,\pm 1/2}$ level is higher than the energy of the ${}^7F_{0,\pm 3/2}$ and the ${}^7F_{0,\pm 5/2}$ levels, the splitting could just as well be inverted. In the experiments carried out in this report this matter is not important.

2.3.1 Qubit construction

The first step in constructing the qubit is to put all ions in the same state, i.e. a pure state. This starts with a few steps of optical pumping that will make manipulations of the $|0>$ and the $|1>$ states easier. To make manipulations without interference from other ions nearby in frequency the interfering ions should be optically pumped to the auxiliary state.

The wide spectral holes around the states of the qubit are needed in order to make the whole qubit experience the same pulse area. The spectral intensity variations over the qubit should be negligible if for instance a π-pulse is applied. To achieve this, wide holes are burnt around the two qubit states and the π-pulse is made short. If the pulse is short enough it will gain bandwidth and the spectral intensity variation over the qubit will decrease.

The gain in bandwidth comes from the *Heisenberg* limit

$$\Delta\nu \cdot \Delta\tau \geq k \tag{2.27}$$

where $k = 0.441$ for *Gaussian* pulse shapes [14]. From this equation it is obvious that the bandwidth, $\Delta\nu$, increases when the pulse duration, $\Delta\tau$, decreases.

It is also necessary to make the spatial intensity variations over the qubit small. This can be achieved by using different beam diameters for the different steps of the construction sequence or by using clever detection techniques, see section 8.2 on page 44.

The first step of the qubit construction phase is to optically pump 10 MHz wide holes around the $|0>$ and the $|1>$ states, se Figure 2.3 below. This pumping procedure will move all the ions constituting the qubit to the $|a>$ state. The ions that are not part of the qubit are moved elsewhere.

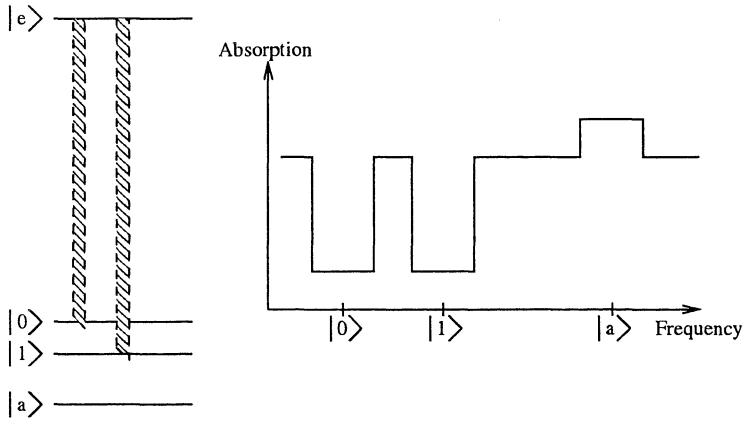

Figure 2.3: Preparing the qubit states. Wide holes are burnt around the $|0>$ and $|1>$ states.

After this first step the $|0>$ and the $|a>$ states are pumped, putting all ions that constitutes the qubit in the $|1>$ state, se Figure 2.4.

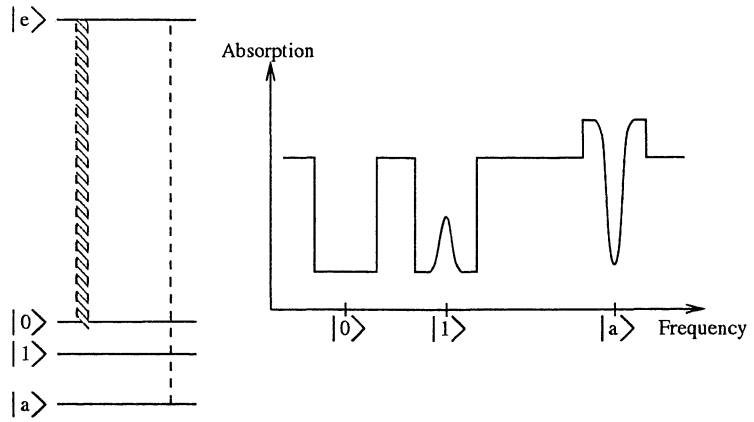

Figure 2.4: Final step of the qubit construction phase. The $|0>$ and $|a>$ states are optically pumped putting all the ions constituting the qubit in state $|1>$.

After this first step of construction the height of the qubit can be expected to be one half of the maximum transmission, see Figure 2.5 for definitions. Of all the ions originally situated at the frequency chosen as the $|1>$ state only one sixth are $|1>$ ions. One half of the ions are of the wrong isotope, the Eu^{3+}-ions in our sample consist of two different isotopes which have different hyperfine level splittings. The rest of the ions have their $|0> \rightarrow |e>$ and $|a> \rightarrow |e>$ transitions at that frequency. There will however be one sixth of the desired ions already situated in the correct $|0>$ state and also one sixth in the correct $|a>$ state. After the optical pumping these ions will be shifted to the $|1>$ state.

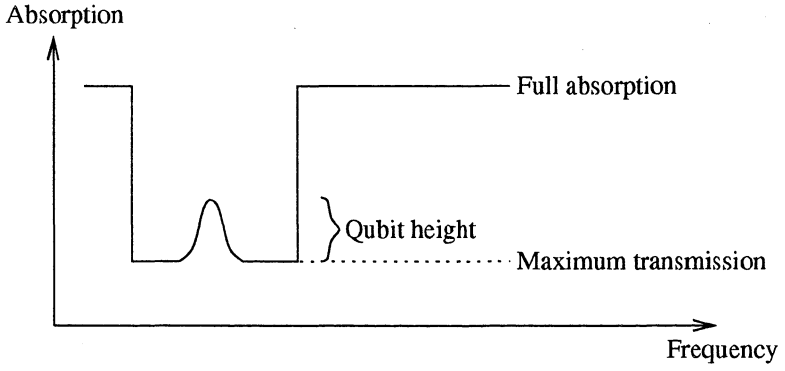

Figure 2.5: Defining the height of the qubit.

The second part of the qubit construction sequence requires two qubits, i and j. The two different qubits will be distinguished by a subscript on their current state, i.e. $|1>_i$ corresponds to the $|1>$ state of ion i. The problem here is to reduce the number of ions in the qubit so that all the ones left can be shifted by the ion-ion interaction.

Consider both qubits to be in their $|1>$ state, upper left of Figure 2.6 shows the qubit j. A π-pulse is applied to $|1>_i$ putting all these atoms in the $|e>_i$ state. The ion-ion interaction will now shift a few of the j-ions away from their original frequency, upper right of Figure 2.6. The remaining j-ions are optically pumped to the $|a>_j$ state, lower left of Figure 2.6. Another π-pulse transfers the i-ions back to their $|1>_i$ state. The shifted j-ions will now return to their original absorption frequency, lower right of Figure 2.6.

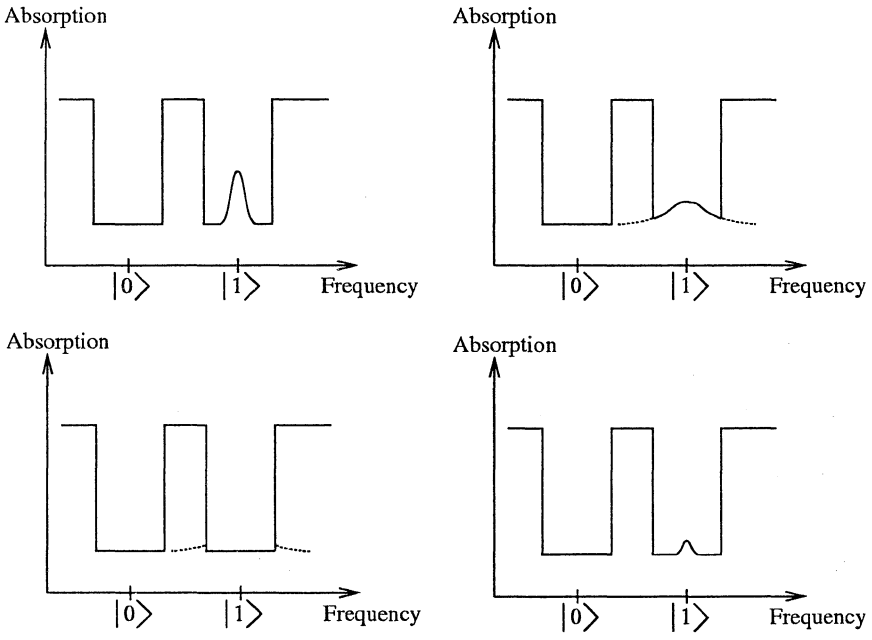

Figure 2.6: The qubit, j, before the refining stage starts (upper left). The qubit after the interacting qubit has been transferred to its excited state some of the ions will be shifted in frequency (upper right). All ions with no frequency shift or only a small frequency shift have been transfered to the auxiliary state (lower left). The interacting qubit is returned to its original state, the shifted ions return to their original absorption frequency (lower right).

The next step is to transfer all the j-ions to their $|e>_j$ state using a π-pulse. This will cause a frequency shift of those i-ions that shifted the j-ions. Optical pumping is performed on the i-ions putting the non-interacting ions in the $|a>_i$ state. The j ions are transferred back to the $|1>_j$ state [13].

What now remains are two qubits that have a mutual interaction. If one qubit is put in its excited state the ions in the other qubit will be shifted out of resonance.

2.3.2 The Controlled-NOT operation

One of the fundamental operations required in the making of a quantum computer is the *Controlled-NOT* operation. The C-NOT operation is a universal gate. It uses one qubit as control bit and one as a target bit. If the control bit is $|1>$ it will perform a NOT operation on the target. If the control bit is $|0>$ nothing happens to the target bit.

Consider j to be the control bit and i to be the target bit, both of these might be in any superposition of their $|0>$ and $|1>$ states. The following steps perform a C-NOT on the two qubits [13].

1. π-pulse on $|0>_j$ - $|e>_j$
2. π-pulse on $|0>_i$ - $|e>_i$
3. π-pulse on $|1>_i$ - $|e>_i$
4. π-pulse on $|0>_i$ - $|e>_i$
5. π-pulse on $|0>_j$ - $|e>_j$

If the controlling qubit, j, is in its $|0>$ state the target qubit will be shifted out of resonance by the ion-ion interaction after step 1. In this case steps 2 to 4 will not change the state of the i-ion. If the control qubit is in state $|1>$ the j-ions will not be excited by step 1. If the target qubit is in state $|0>$ it will be put in state $|1>$ by step 2 and 3. If it originally was in the $|1>$ state it is put in the $|0>$ state by step 3 and 4.

In actual computations the control qubit will most likely be in a superposition of its two states, which is also true for the target bit. What now happens is that the C-NOT gate will put these two qubits in an entangled state.

The scheme given above can be generalised to a multi-qubit C-NOT gate by repeating the first and last step for all the control qubits.

Chapter 3

Equipment

3.1 The CR-699 ring dye laser

A *Coherent Ring dye laser model 699-21* was used throughout the experiments. It was pumped by an Ar^+-ion laser (*Coherent Innova 400*). The dye in the laser was *Rhodamine 6G*. See Figure 3.1 for a schematic description of the dye laser. According to [15] the laser can give an output power of 0.5 to 1 W in single mode operation. In order to measure the wavelength of the laser a wavelength meter was used [16].

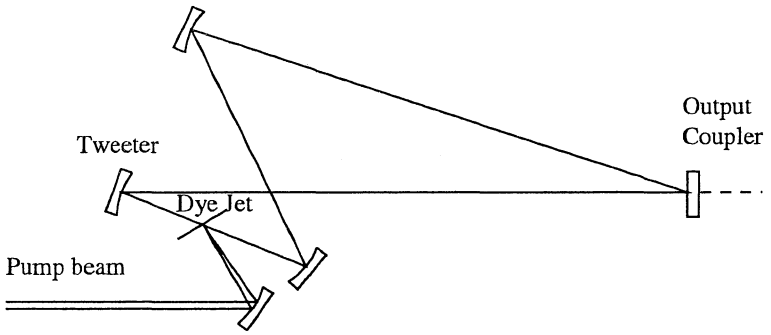

Figure 3.1: Schematic picture of the mirror and beam configuration of the CR-699 ring dye laser

3.1.1 Frequency locking

The dye laser frequency is locked to a temperature stabilised *Fabry Pérot* reference cavity. By tilting a glass plate inside the reference cavity it is possible to alter its optical path length.

The transmission through the reference cavity is described by the *Airy function*

[17]. By tilting the glass plate you can choose the transmission through the cavity. To get a useful error signal the cavity's optical length is adjusted so that half the maximum intensity is transmitted.

At 50% transmission the position on the *Airy function* is at the point where the derivative is the greatest. Frequency modulating the laser radiation thus gives a maximum signal at this point and this signal maximum can be used as a lock point. Deviations from this reference level are used as the error signal. The laser's cavity length is adjusted accordingly by moving the tweeter mirror (mounted on a piezo element) and tilting a Brewster plate according to the error signal.

3.1.2 Frequency tuning and scanning

In order to tune the laser frequency the length of the reference cavity is changed. When the glass plate inside is tilted the transmission will deviate from the reference level. This induced error signal is fed to the laser's stabilising unit. The laser adjusts its own cavity length in order to maintain the correct error level. The result is that the frequency is changed. If the glass plate is given a continuous tilt the laser's frequency is scanned.

When tuning the laser over larger frequencies a *Lyot filter* (birefringent filter) is used to adjust the laser cavity transmission profile.

3.1.3 Stability

According to [15] the frequency stability of the dye laser is on the order of 30 MHz/hour. Laser stability is of outmost importance since a shift of 30 MHz is equal to the smallest *hfs*-splitting in our crystal, see Table 3.1 on page 22. The stability was tested by hole burning.

The crystal was submerged in liquid helium, cooled to the λ-point. A spectral hole was burnt in the inhomogeneous profile. Then we monitored the position of the hole by recording a transmission spectrum by changing the laser frequency using the internal scan function of the laser. On consecutive scans the hole changed position due to the frequency drift of the laser.

The result is shown in Figure 3.2 and it is obvious that the frequency stability is around 30 MHz/hour. In the figure the position of the hole relative its original position is plotted versus time. The experimental set-up for this experiment can be seen in Figure 5.1 on page 31.

3.2 The $Eu^{3+} : Y_2SiO_5$ crystal

The material used for these experiments was an Eu^{3+}-doped Y_2SiO_5 crystal. The crystal was cylindrically shaped with a diameter of roughly 5 mm and a

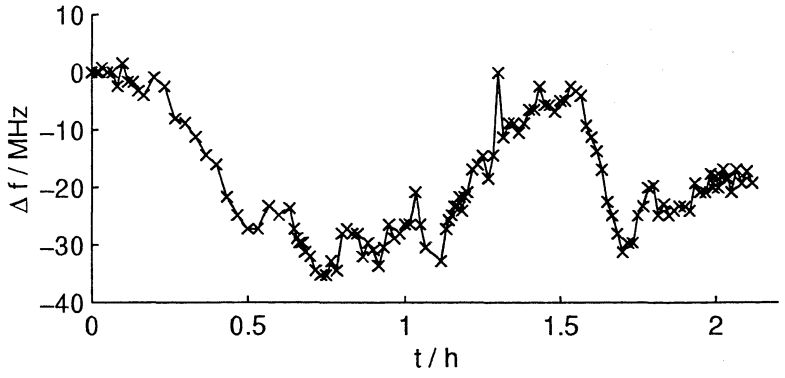

Figure 3.2: Long-term stability of the dye laser. The position of a hole relative its original position is plotted versus time.

length of 10 mm. The dopant level was $\approx 0.1\%$.

The reason for choosing this material was its hyperfine level splitting. The energy differences and the hyperfine level lifetimes, several hours, are very suitable for learning how to create the qubits.

3.2.1 Crystal structure

Y_2SiO_5 is a monoclinic biaxial system with a C_{2h}^6 ($C\,2/c$) space group of the *Laue* class $2/m$ [18]. The lattice parameters are: $a = 1.042$ nm, $b = 0.6721$ nm, $c = 1.249$ nm and $\beta = 102°39'$. There are eight Y_2SiO_5 groups in each unit cell [19]. The indices of refraction are: $n_a = 1.772$, $n_b = 1.773$ and $n_c = 1.793$.

The Eu^{3+} ions will substitute for the yttrium-ions which have two different sites in the crystal structure. This gives two different type of active centres (henceforth called S_1 and S_2).

3.2.2 Absorption profile

When the Eu^{3+}-ions randomly replaces the Y^{3+}-ions in the crystal they will distort the crystal structure. This will lead to an inhomogeneous broadening of the Eu^{3+}-ions' absorption line. In rare-earth-ion-doped crystals at liquid helium temperatures the homogeneous line width could be on the order of kHz and the inhomogeneous on the order of GHz. This is the case for both Y_2SiO_5 and $YAlO_3$.

The homogeneous line width is close to the natural broadening caused by the limited lifetime of the upper state, i.e. the *Heisenberg limit*. The reason for the narrow homogeneous line width in Eu^{3+} is the fact that the transition ${}^7F_0 \leftrightarrow {}^5D_0$ occurs within the $4f$-shell of the atom. The $4f$-shell lies deep within

the ion surrounded by outer electrons and therefore the $4f$-electrons are shielded from disturbances from the surroundings. The crystal field is however different at the two sites. This leads to different absorption frequencies for them, 579.879 and 580.049 nm at 6 K for S_1 and S_2 respectively [20].

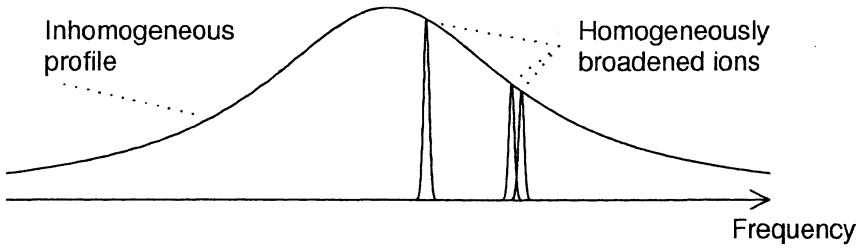

Figure 3.3: Inhomogeneous and homogeneous line broadening.

The ground and the excited levels of the ions are split into hyperfine states. Both the ground and the excited levels have had their degeneracy broken by the electric field of the crystal, they are *Stark*-shifted and broken into three two-fold degenerate levels. Table 3.1 lists the energy separations in these hyperfine states, for the two different isotopes as well as for the two different sites [20][21]. The ${}^7F_0\,\nu(\pm 1/2 \leftrightarrow \pm 3/2)$ corresponds to the energy difference between the $|0>$ and the $|1>$ qubit states.

	S_1, ${}^{151}Eu$	S_1, ${}^{153}Eu$	S_2, ${}^{151}Eu$	S_2, ${}^{153}Eu$
${}^5D_0\ \nu(\pm 1/2 \leftrightarrow \pm 3/2)$ / MHz	75	194	63	160
${}^5D_0\ \nu(\pm 3/2 \leftrightarrow \pm 5/2)$ / MHz	102	260	108	274
${}^7F_0\ \nu(\pm 1/2 \leftrightarrow \pm 3/2)$ / MHz	34.5	90.0	29.5	76.4
${}^7F_0\ \nu(\pm 3/2 \leftrightarrow \pm 5/2)$ / MHz	46.2	119.2	57.3	148.1

Table 3.1: The hyperfine level splitting of $Eu^{3+} : Y_2SiO_5$ isotopes.

Our sample was made of natural Eu which has a 44.8% abundance of ${}^{151}Eu$ and 52.3% abundance of ${}^{153}Eu$. We used only S_2 of ${}^{151}Eu$ in our experiments due to its longer homogeneous dephasing time.

3.2.3 Coherence

As previously described you need to use a material with a long homogeneous dephasing time, T_2, in order to build a working quantum computer. $Eu^{3+} : Y_2SiO_5$ has the longest optical dephasing times found in rare-earth-ion-doped crystals [20].

The main reason for the long dephasing time found in crystals like $Eu^{3+} : Y_2SiO_5$ and $Eu^{3+} : YAlO_3$ is the location of the excited electron. The $4f$-electrons lie inside the ion's outer shells. The electron interaction with the environment will therefore be very small. $Eu^{3+} : Y_2SiO_5$ has a longer homogeneous dephasing time than $Eu^{3+} : YAlO_3$ due to the weaker nuclear interaction.

	S_1	S_2
λ / nm	579.879	580.049
Γ_{inh} / GHz	8.6	5.6
T_1 / ms	2.0	1.7
T_2 / ms	0.477	0.822

Table 3.2: Transition wavelengths, λ, inhomogeneous line widths, Γ_{inh}, upper state life times, T_1, and homogeneous dephasing times, T_2, for the two sites.

In natural Si only the 4.7% abundant ^{29}Si has a nuclear moment, $-0.56\,\mu_N$. Its value is small compared to the 100% abundant ^{27}Al's moment of $3.64\,\mu_N$. Unlike ^{27}Al ($I = 5/2$) ^{29}Si ($I = 1/2$) does not experience any nuclear electric quadrupole interaction. Spin-flips caused by the $Eu \leftrightarrow Al$ interaction leads to a phenomenon called spectral diffusion [21], i.e. shorter homogeneous dephasing time than Y_2SiO_5 which essentially does not experience this type of spectral diffusion.

3.3 Cooling system

The crystal is submerged in liquid helium inside a cryostat (*CRYOVAC*). In order to minimise heat transfer into the helium it is placed inside a high vacuum container. The vacuum is surrounded by liquid nitrogen, which in turn is surrounded by another layer of vacuum.

Three optical glass windows separate the sample chamber and the outside environment on each side, there is no liquid nitrogen between the optical windows. Between the windows there is vacuum and therefore we have roughly 4% reflection at each interface of which there are five. Thus the power decreases by roughly one fifth by passing through the windows into the cryostat. The refractive index of liquid helium is 1.408 [22], this gives a reflectance on the order of 1% on the helium-crystal interface, this is about the same reflectance as on the helium-glass interface.

Another problem with the cryostat is that helium bubbles will act as lenses and change the focussing and direction of the laser beam when they pass through the beam, see page 29. One way of getting around this is by cooling the helium to the λ-point, at 2.2 K, where it becomes a superfluid and the bubbles disappear.

3.4 Modulators

3.4.1 Acousto-optic modulators

In the experimental set-ups we have used acousto-optic modulators (AOMs) to create the small frequency shifts needed in the pulse sequences as well as for switching the pulses on and off. The AOMs (*ISOMET 1205C Bragg cells*) shift the incoming photon's frequency and direction by giving them extra energy via phonon (acoustic wave) absorption.

The light is refracted as in a grating with the difference that the 1^{st} order is shifted in frequency relative to the 0^{th} order. The shifts gained in our AOMs were tuneable between 60 and 100 MHz. For more information regarding efficiency and stability see [23] and for theory [9].

3.4.2 Electro-optic modulators

An electro-optic modulator (EOM) can in principle be regarded as a half-wave plate (it is also possible to get elliptically polarised light from it) that you are able to switch on and off. If used in conjunction with a polarising prism it will change the intensity of the transmitted laser beam. For a more thorough description see [9].

The EOM is a crystal that is uni- or biaxial. The indices of refraction changes when an electric field is applied. If the incoming light is polarised in a 45° angle to the axes of the two different refractive indices the light will change polarisation. If the difference in path length is equal to half a wavelength the polarisation will be turned 90°.

By adjusting the voltage over the crystal you can achieve either one of two linearly and orthogonally polarised states (or elliptically polarised). When a polarising filter (prism) is placed behind the crystal the transmitted light intensity varies with voltage. The maximum on-off ratio achieved in our set-up was around 250:1 which was a little bit too high for our purpose. The voltage was adjusted to give an on-off ratio of 50:1.

3.4.3 Mechanical shutters

In order to block the beam paths into the cryostat a few mechanical shutters were used. They are in principle electrical relays with attached blocks. Switching of the relay causes the arm to flip in or out of the beam path, thus enabling a total block of the beam paths.

When the shutter flips in position a certain amount of vibration sometimes interfered with the laser cavity stabilisation and thus increased the laser drift. To get around this we placed the shutters on floor mounts (or on another table) outside the optical table where the laser was placed.

3.5 Detection

We used three different types of photodiodes in the experiments and one photomultiplier tube.

Hamamatsu, *S1223* Two PIN-photodiodes with homebuilt amplifying/offset units. These photodiodes are not that fast and have a cut-off frequency of 30 MHz (biased). In order to get a lower noise level we turned off the bias.

Hamamatsu, *S3399* A rather fast PIN-photodiode with a cut-off frequency of 100 MHz. It has a higher dark current than *S1223* and it is not equipped with any amplifier. Used in the signal-to-noise experiments, see section 4 on page 26.

Electro-optics Technology, *ET2010* A very fast PIN-photodiode, rise and fall time less than 1 ns and a cut-off greater than 400 MHz. Used in beating measurements when establishing the different voltages given to the AOMs, see page 35.

Electron Tubes, *EMI 9816QB* Photo multiplier tube used in the signal-to-noise and hole burning experiments.

3.6 Electronics

In the experiments a wide range of pulse, signal and waveform generators were used. In addition to the commercial systems listed below a variety of current and voltage generators were used.

Stanford Research Systems, *DS345* Arbitrary waveform generator used to generate frequency chirps and pulses. Maximum output amplitude is 5 V.

Stanford Research Systems, *DG535* Digital delay / Pulse generator used to create pulse trains to the different AOMs and the triggering of other units. It has a TTL output.

Hewlett Packard, *8013B* Pulse generator able to give one or two identical pulses, with an amplitude greater than the TTL-level.

Tektronix, *FG 504* Function generator with high output amplitude (15 V).

Tektronix, *TDS 540* A fast oscilloscope, 1 GS/s, used for information sampling and storing. Usually working in *High-resolution*-mode.

Chapter 4

Signal-to-noise considerations

In all kinds of detection a certain amount of noise will be present. An important aspect of these experiments is to increase the signal-to-noise ratio.

A common principle for reducing noise is to repeat the measurement several times and then average. In most parts of the experiments this was not feasible. In many cases we only had one opportunity to make the measurement. Too many measurements would have destroyed the prepared structures.

4.1 Sources of noise

In our experiments there are a few well-known sources of noise. First of all is the *thermal noise* in the detectors. The thermal movements of the electrons in the photocells cause this. Typical values of this noise are given by the *Noise Equivalent Power* (NEP), i.e. the power that will give a signal of the same amplitude as the thermal noise. Typical values for our photodiodes are 10^{-11} W. Since we are detecting transmission of laser beams with powers in the mW-region this effect will be negligible.

One factor that is important is the *power noise* from the lasers. It starts with power noise in the Ar^+-laser which in turn is magnified by the dye laser. The result is that the power from the laser varies by roughly 5%. This is the largest source of noise and fortunately one that quite easily can be dealt with.

The Ar^+-lasers power supply also gives a 300 Hz noise that travels through the optical tables to the detectors and into the Ar^+-laser. Other electromagnetic sources (such as radio, 107 MHz) of noise is taken up in the coaxial cables used for signal transmission.

When submerging the crystal in liquid helium we sometimes got very noisy signals. This happened when there were many bubbles in the liquid.

4.2 Reducing noise

The different sources of noise could not all be dealt with in the same way. The largest source is the power noise from the lasers. It was also quite easy to discriminate. The thermal noise in the detectors was considered insignificant and to avoid getting noise into the signal cables we used shielded cables.

When measuring the fluorescence with the photomultiplier it acted as a low-pass filter and the high frequency noise was discriminated. The low frequency power noise was, on the other hand, not that easy to take care of.

4.2.1 Oscilloscope sampling

Our oscilloscope (*TDS 540A*) can operate in 5 acquisition modes. Below is a short description of them, for further information read [24].

Sample The oscilloscope records the first sample in each sampling interval. Each sample is stored with 8 bits, which gives 256 different values for the signal level. Preferable use is with fast signals.

Peak Detect In each sampling interval the most extreme value is saved. Storing the maximum and minimum value is switched between intervals. This mode is used for detecting glitches and aliasing.

High Resolution The stored value is an average over all the samples in each sampling interval. This causes the apparent noise to be significally reduced, see Figure 4.1. The bit length, i.e. the number of significant bits, of each stored value increases with the time base duration, for time bases less than 400 ns it is 8 bits and the bit length steadily rises with time base to 15 for a time base of 5 ms and longer.

Envelope Uses three acquisitions from a single source. On each occasion it uses *Peak detect* mode and stores the maximum and minimum values in each interval. This lets you record a waveform that shows the extremes in variation over several acquisition.

Average Uses the average value of many acquisitions in *Sample* mode. Very useful for reducing apparent noise in repetitive signals. This mode gives a higher bit length of the stored values than *Sample* mode.

In the experiments we were carrying out the time scale was not that short (μs to ms) and we only had the opportunity of doing single acquisitions. The best sampling mode of the oscilloscope was then *High Resolution* since this gives a low-noise signal with high bit-resolution. For a comparison between *Sample* and *High Resolution* see Figure 4.1.

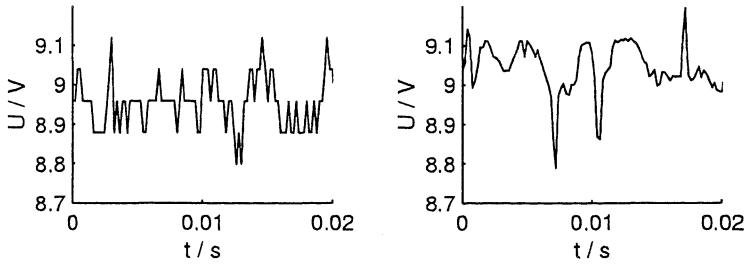

Figure 4.1: Illustration of the different resolutions with *Sample* (left) and *High Resolution* (right) on similar signals.

4.2.2 Power fluctuations in the lasers

A small experiment was carried out to see how much of the noise came from power fluctuations in the dye laser. The experiment consisted of the lasers, one beam splitter and two identical detectors, *S1223*, se Figure 4.2.

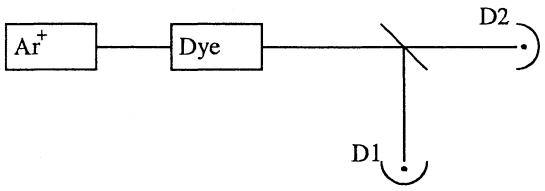

Figure 4.2: Experiment set-up: Power noise.

Different time scales were tested and the results were clear in the respect that the major part in noise came from power fluctuations. In Figure 4.3 below the oscilloscope was using *High Resolution* mode.

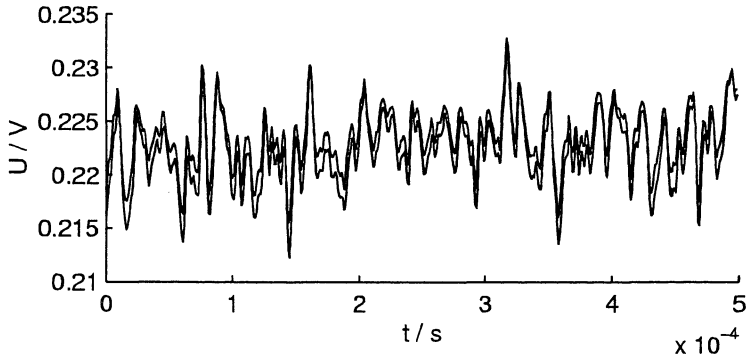

Figure 4.3: The two different photodiodes records the same signal. This clearly illustrates that the power fluctuations in the lasers are a primary noise source.

4.2.3 Detectors

Since the NEP of the photodiodes are insignificant we did not think that cooling the diodes would reduce the noise in any significant way. The two photodiodes used in the experiments were identical. We adjusted the offset levels with the amplifying unit to equal levels. To get the same response times from the two diodes we put a neutral damping filter in front of the reference diode to get the same intensity on both diodes. The response time of the photodiodes is connected to the current leaving the diode. A large current gives a long response time. This effect is also amplified by the amplifying unit.

The signal cables used for transmitting the signal from the diodes to the oscilloscope were shielded coaxial cables. They were of equal length and to let them experience the same noise they were placed side by side. In this way any noise induced in the photodiodes and the cables can be reduced by dividing the signals from the two matched photodiodes. This also takes care of the power fluctuations in the laser light.

4.2.4 Bubbles

Bubbles in the liquid helium will act as negative lenses, gaseous helium's refractive index is close to 1 while it is 1.4 for liquid helium. If the bubbles are small this will not present a major problem but one can assume that it causes some noise. Large bubbles will however change the divergence and/or direction of the beam. A typical recording with large bubbles can be seen in Figure 4.4 below.

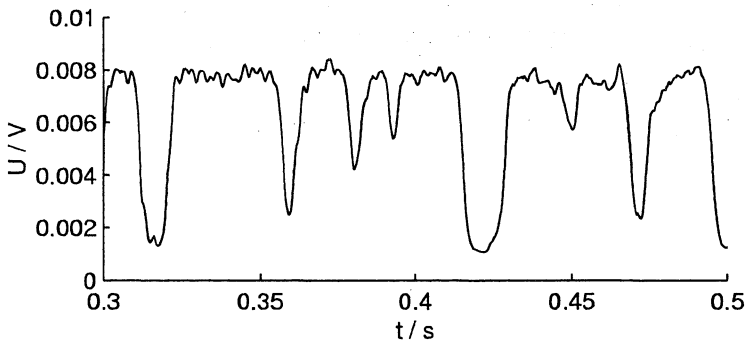

Figure 4.4: Large helium bubbles can clearly bee seen on the recorded signal.

If the pressure inside the cryostat is lowered to around 50 Pa the temperature of the liquid decreases to 2.2 K. The liquid reaches the λ-point and becomes superfluid. As long as it remains a superfluid there will not be any bubbles.

Chapter 5

Hole-burning

When constructing a qubit one needs to know the energy differences between the hyperfine levels in the Eu^{3+}-ions. This information can be obtained by doing hole burning experiments and looking at the side- and anti-hole structure as in [20].

5.1 Experimental set-up

In this hole burning experiment we decided to use two beams with different diameters. One large for the burning sequence and one smaller for probing. Achieving different beam diameters was done by putting a telescope in the probe beam, the set-up can be seen in Figure 5.1.

Instead of AOMs mechanical shutters were used for switching the beams on and off since these give a higher on-off ratio. The main drawbacks of the mechanical shutters are slow operation and vibrations. The intensity of the probe beam was roughly 2 orders of magnitude lower than the burning beam. A photomultiplier tube was used for detection of the fluorescence from the crystal. This was thought to give a signal with lower background noise.

In the experimental set-up the beam coming out of the dye laser travels through a beam splitter. About 70% of the intensity is deflected towards the mechanical shutter, *SA*, controlling the burning beam.

The 30% that is left of the beam passes the second mechanical shutter, *SB*, a telescope that decreases the beam diameter and a spatial filter, *Sp. f. 0.1 mm*. This part of the beam is used as the probing beam. The reasons for using a smaller beam diameter of the probing beam is to make the beam probe an area in the crystal that has been completely burnt by the wider burning beam. The spatial filter is used to give a nice gaussian intensity distribution of the probe beam.

The two beams are overlapped on a glass plate. The major part of the burning

beam passes straight through the glass and only a minor part of the probing beam is reflected. This leads to the intensity difference between the two beams of roughly two orders of magnitude.

Two beams leave the glass plate. One goes through the crystal inside the cryostat and hits the signal diode. The other one passes a variable neutral density filter, *Var. ND*, and hits a reference diode. The density filter is adjusted so that both photodiodes experiences the same intensity in the probing sequence.

A photomultiplier tube, *PMT*, is placed perpendicularly to the beam that passes through the cryostat.

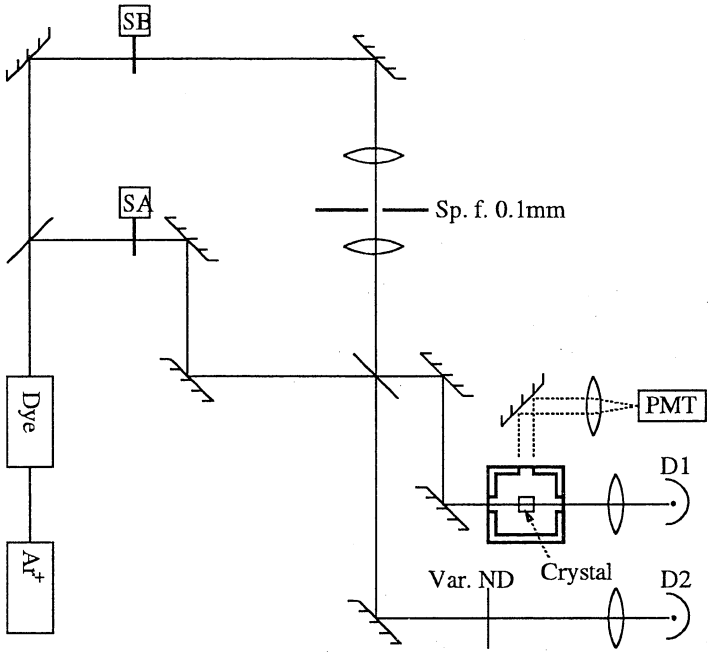

Figure 5.1: Experimental set-up: Hole burning. The set-up consists of the Dye and AR^+ lasers, one 70/30 beamsplitter, two mechanical shutters (*SA* and *SB*), one telescope and spatial filter, one glassplate, the cryostat with crystal sample, one photomultiplier tube (*PMT*) and two photodiodes (*D1* and *D2*).

5.2 Results and discussion

The signals shown in the right picture in Figure 5.2 are the best results achieved in this part of the experiment. The left and top pictures are a theoretically modelled spectrum, see appendix A on page 49.

While doing these experiments the helium was cooled regularly to the λ-point. The pressure inside the helium chamber increases with time. The temperature rises slowly, but it takes some time before bubbles emerge. The reason for

not pumping continuously on the helium was that the vacuum pump caused vibrational and acoustical noise in the dye laser.

Unfortunately the fluorescence signal recorded by the photomultiplier did not give the expected low-noise signals. The power fluctuations in the laser light could clearly be seen in this signal. The signal from the PMT is however hard to correct with the reference diode since the fluorescence signal acts like a low pass filter with respect to the intensity variations of the laser input. The lowest noise signal is then the quotient of the signals from the two photodiodes. This signal has also been divided with a pre-hole burning spectra, to give a straight line. The PMT was however used when we looked at the satellite lines on the slope of the inhomogeneous profile, see Figure 8.1 on page 44.

As can be seen our experimental spectra bears close resemblance to the theoretically modelled one. To discriminate the noise the data has been low pass filtered. Our results are quite similar to those presented in [20].

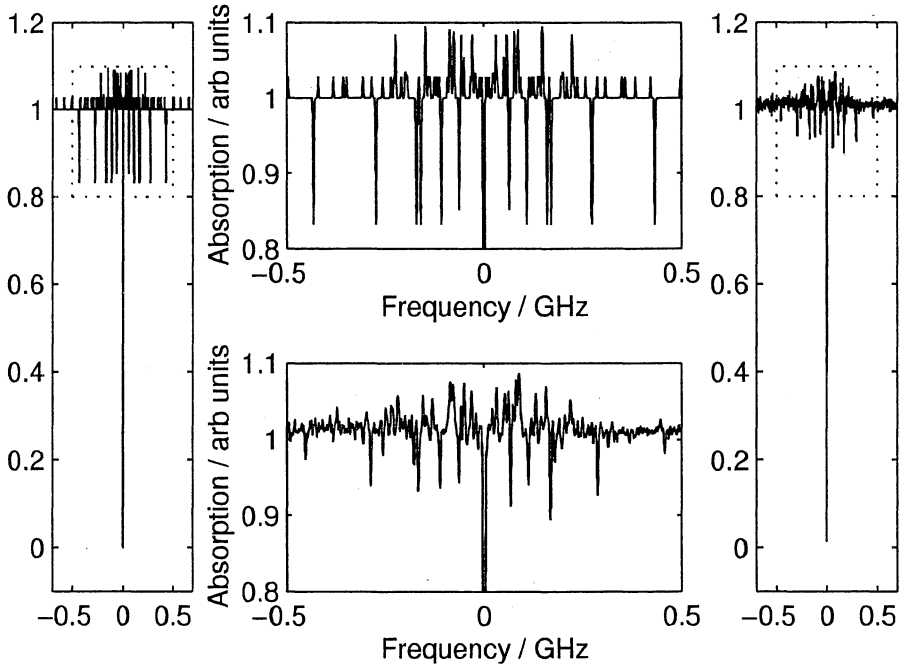

Figure 5.2: A theoretically calculated spectrum (left and top) and its experimental counterpart (right and bottom).

One difficulty in these kinds of experiments is the probing of the hole structure. One wants to probe the sample at a place where it has been completely optically pumped. If the probing beam has a larger beam diameter than the burning beam it will hit places in the sample where the ions have not been optically pumped. The solution is then instead to make the probe beam's diameter smaller than the pumping beam. It will then pass through an area in the sample where all the ions have been optically pumped.

Another way of getting a low noise (practically zero background) signal is to use a *holographic detection* technique [25]. This technique uses two burning beams (phase coherent) that hit the sample from two different angles. This will produce a burnt grating in the sample.

The probing beam comes parallel to one of the burning beams and the signal beam will be defracted parallel to the other burning beam. Since the detector only will look at defracted light the background will be insignificant.

However, the holographic technique is not very useful when constructing qubits. The qubit has to be both spectrally and spatially separated from the surrounding ions. The spectral part could just as easily be achieved with the holographic technique. The spatial separation cannot be achieved since the two burning beams will produce a grating structure in the sample.

If the technique using two beams is employed, as we have done, there is a difficulty in the overlapping of the two beams. In this experiment the overlapping took place on a glass plate. The two beams are aligned at the glass plate as well as at long distances.

The overlapping of the beams and the spatial variations of the intensity are also more general problems in the design of the qubits. In the hole burning experiment this has been solved, as stated above, by using two unfocussed beams. One large beam for the burning pulse and one with smaller diameter for the probing. Another technique that might give better signal-to-noise ratio is using a pinhole at the detection side. It is outlined more in section 8.2 and used in for instance [26].

Chapter 6

Qubit construction

This experiment is an attempt to construct a single qubit according to the scheme given in section 2.3.1.

Since the excited state consists of three different hyperfine levels the scheme has to be slightly modified. If the original construction scheme is implemented it turns out that an extra anti-hole will appear in the wide hole around the $|0>$ state. To get rid of this the state $|a>$ is also pumped during the first step of the preparation procedure.

6.1 Experimental set-up

In this experimental set-up, Figure 6.1, we have used AOMs to shift the laser's frequency and one EOM to vary the intensity of the beam. Two beams were used in order to cover the frequency range needed.

One beam travels through a single AOM that gives a fixed frequency shift in -1^{st} order. This beam is used to excite the $|a>$ state. The other beam travels through a double AOM system in which the frequency can be shifted by 120 – 200 MHz without beam deviation using the -1^{st} order in both AOMs. This beam was used for manipulating the $|0>$ and the $|1>$ state. It was also the beam employed for probing, using its whole tuneability in 80 μs.

The reason for using the -1^{st} order can be understood from the values given in table 3.1 on page 22. If we had chosen the 1^{st} order the frequency shift would have been positive. The double AOM would then have been used for manipulating the two higher states with the energy separation of 57 MHz stretching the AOMs tuneability to the limit. The single AOM would have needed to shift the light by around 100 MHz and the double AOM by 125 to 190 MHz, see Figure 6.2 below.

Choosing the -1^{st} order gives shifts of 90 and 145 to 185 MHz, for the single and the double AOM respectively, see Figure 6.3. This is a lot closer to the

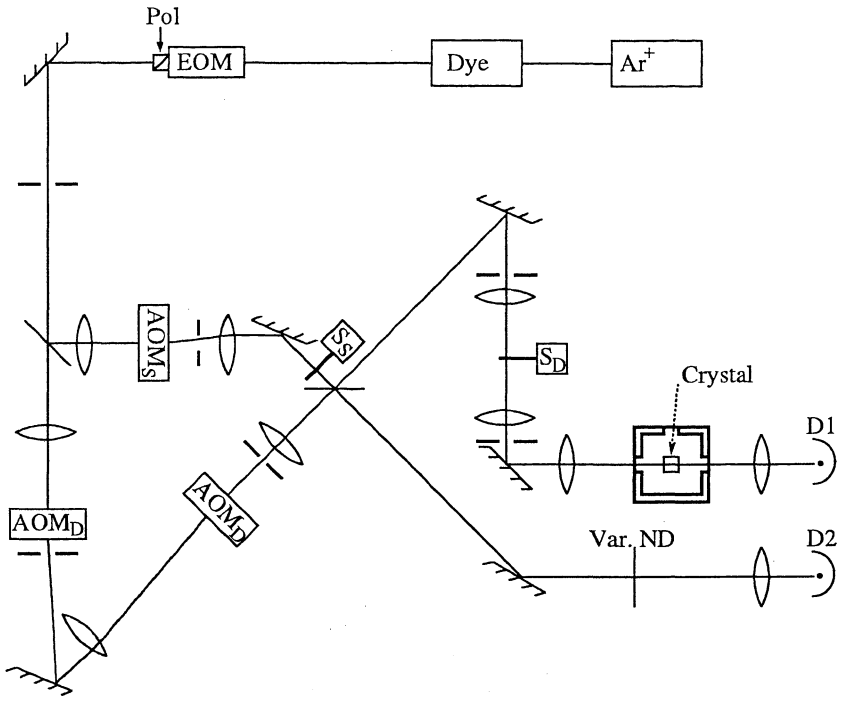

Figure 6.1: Experiment set-up: Qubit construction. The set-up consists of: dye an Ar^+-ion lasers, one electro-optic modulator (*EOM*) and polarizer (*Pol*), one 70/30 beamsplitter, a single acousto-optic modulator (AOM_S), a double acousto-optic modulator system (AOM_D), a 50/50 beamsplitter, two mechanical shutters (S_S and S_D), the cryostat with sample and two photodiodes (*D1* and *D2*).

optimum for the AOMs and therefore the chosen order.

To further increase the on-off ratio mechanical shutters were used. This was done to avoid light leakage into the crystal, i.e. unwanted hole burning. These were opened about 50 ms before the AOMs were turned on.

In order to get the right frequency shifts between the two beams beating experiments were conducted. This was done by putting the fast photodiode where the two beams overlapped. The signal was analysed by the oscilloscope's FFT function.

To get the desired pulse sequence, Figure B.1 on page 53, a lot of pulse generators were used, the connections between them can be seen in Figure B.2 on page 54.

The power of the laser beams before the cryostat was 8 mW and 21 μW for the burn and probe pulses respectively. At the reference diode it was 4.7 μW for the probe pulse.

The final set-up can be seen in Figure 6.1. The laser beam leaving the dye laser first travels through the *EOM* in which the intensity is decreased by a factor of

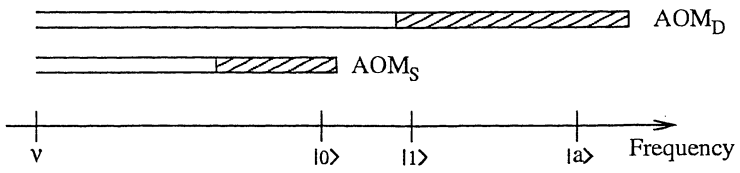

Figure 6.2: AOM shifts using the 1^{st}-order of diffraction. The tuneability of each AOM is the region with stripes. The shift needed using this order stretches the AOMs capabilities to the limit.

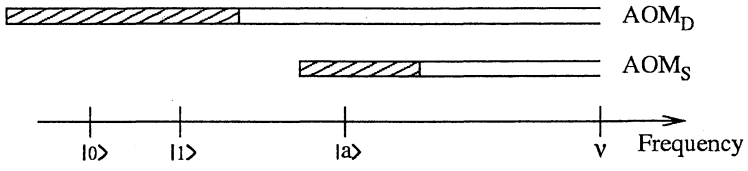

Figure 6.3: AOM shifts using the -1^{st}-order of diffraction. The tuneability of each AOM is the region with stripes. In this case the shifts are well within the tuneability of the AOMs.

50 if it is switched on, which is done when probing. The polarising prism, *Pol*, keeps the polarisation angle of the light from changing when the EOM is turned on.

The beam passes an iris and then a beam splitter where approximately 30% is deflected towards the AOM_S and the mechanical shutter controlling this beam path. The rest of the light passes through the beam splitter and enters the double AOM system, AOM_D. The two laser beams are overlapped on a 50/50 beam splitter.

One of the beams leaving the second beam splitter goes through a telescope that changes the diameter of the beam. In the middle of the telescope (in the focus) the second mechanical shutter is placed, S_D. This placement gives a very high on-off ratio. The beam is focussed to a beam waist of 30 μm, the beam diameter on the ends of the crystal is around 42 μm giving an intensity difference of 2 along the longitudinal axis of the crystal. The outgoing beam is focussed on the signal diode, *D1*.

The other beam that leaves the second beam splitter goes through the variable neutral density filter, *Var. ND*, and hits the reference diode, *D2*. The density filter is adjusted to get equal intensity, at zero absorption, of the two beams during the probing.

6.2 Results

As the first part of these experiments we did a preparatory experiment just by burning two 10 – 12 MHz holes separated by 29.7 MHz (around level $|0>$ and $|1>$). After that a burning pulse was directed at $|a>$.

In Figure 6.4 we can clearly see the two burnt holes. The side- and anti-holes of the burn pulse at $|a>$ are also visible. One can clearly see two anti-holes in the $|0>$ hole. The one to the left is our $|0>$ level and the one to the right is some other anti-hole. The anti hole in the $|1>$ hole is of course our desired qubit state $|1>$.

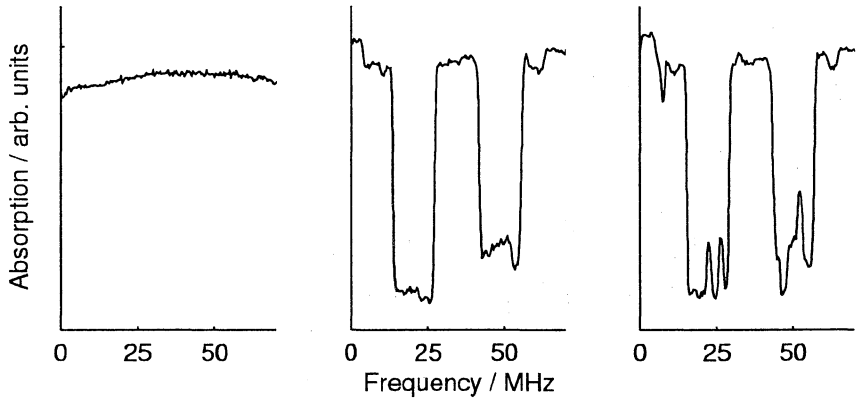

Figure 6.4: Preparatory experiment for qubit construction. Spectrum before the initiation of the first burning sequence (left), between the two burning sequences (middle) and after the burning at $|a>$ (right).

To construct the qubit we pumped two wide holes at $|0>$ and $|1>$, as well as a narrow hole at $|a>$ level. After that a probe is performed and then the last burn sequence at the $|1>$ and $|a>$ are carried out. In the experiment shown in Figure 6.5 the times used for the first burn sequence was optimised to be 600 ms and the second to be 300 ms.

The burning times have to be at least a few times longer than the decay time of the upper state (1.7 ms) if π-pulses are used in the pump sequence. As we could not achieve the power needed for π pulses we increased the burning times to a few hundred ms.

6.3 Discussion

As seen in Figure 6.5 we have constructed one qubit with good signal-to-noise ratio. The height of the qubit is roughly what is expected from section 2.3.1.

The result gained in this experiment could be considerably improved if a crystal

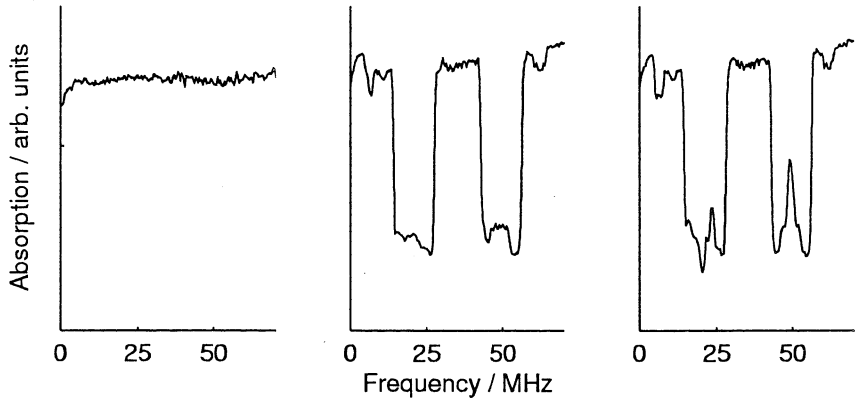

Figure 6.5: A constructed qubit. The left picture shows the spectrum before the pumping process, the middle picture is taken after the initial pumping and the right picture is after finishing the qubit preparation.

doped with only one isotope was available. Unfortunately none was available at our laboratory at the time of the experiment, but it is certainly technologically possible to manufacture single-isotope crystals.

One other improvement is on the detection side where we are considering using a pinhole (se section 8.2) in order to look only at the central part of the beams.

If it turns out that the hyperfine structure (see Figure 2.2 on page 14) is inverted relative to the one we have used, the only major change need to make is to use the 1^{st} diffraction order of the AOMs. All pictures showing the different qubit states will of course be inverted.

Due to the symmetry of the side-/anti-hole structure, see appendix A on page 49, it is not easy to see if we have chosen the correct model. The result shown in the middle picture of Figure 6.5 shows some indication of that the model used can be the wrong one.

The reason for this is that we optically pump all the ground state hyperfine levels at the same time. If the correct model had been chosen the ion constituting the qubit would have moved between the different states, but there should always be one third in each state. This would lead to one peak at $|0>$ and one at $|1>$ with height one sixth.

In the middle picture of Figure 6.5 there seems to be some peaks at the qubit states. The height of these peaks are definitely too small and some structure is also present in Figure 6.4, this indicates that the incorrect model has been chosen. The resulting peak in the right picture of Figure 6.5 is, on the other hand, about one half and this indicates that the correct model has been chosen. From these results I cannot say with certainity that the model used is either the correct or the incorrect one.

Chapter 7

Ion-ion interaction

One of the most important factors, regarding the possibilities for this quantum computing scheme, is that ions that are separated in frequency can interact in a controlled way, see section 2.2 on page 13.

As we have chosen to start the experimental work with Eu^{3+} in Y_2SiO_5 it will not be very easy to show the desired behaviour. If this experiment is carried out with $YAlO_3$ as a host crystal it might be easier since the excitation-induced frequency shifts are expected to be larger in this material.

7.1 Experimental set-up

The experimental set-up for this experiment is very similar to the one used in the qubit construction, se Figure 6.1 on page 35. The major difference is that another laser must be used. This laser is used to excite ions at a frequency roughly 1 GHz away from the original laser's frequency. It is then possible to study the effects of the excitation induced frequency shifts on the qubits.

The large difference in frequency is needed in order to make sure that effects seen are not connected to the side-/anti-hole structure. Since this structure covers about 1 GHz around a single hole the difference between the two laser should be greater than this.

Since the two beams should overlap spatially we made the laser beams conter-propagate inside the cryostat. The best way is of course to make them anti-parallel in order to be able to do measurements while this excitation beam is switched on.

Another thought is to enter the sample perpendicular to the original laser beam. In this way you should also be able to make a small quantum computer at the point where the two beams overlap. One would then of course need some imaging technique on the detection side so that you only look at the overlap between the two beams.

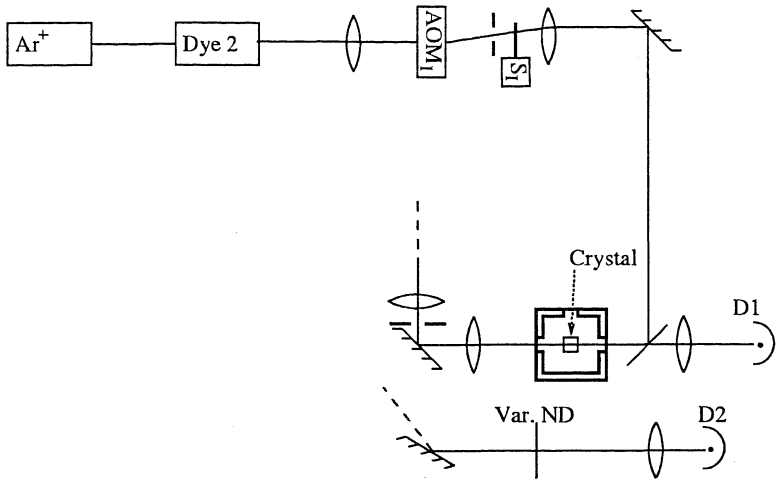

Figure 7.1: Experiment set-up: Ion-ion interaction. The major part of the setup can be seen in Figure 6.1. The additions made in this set-up is another dye laser system, one acousto-optic modulator (AOM_I), one mechanical shutter (S_I) and one 50/50 beamsplitter.

The experimental set-up shown in Figure 7.1 is the additions to the equipment used in the qubit construction experiment. The additions consist of another dye laser pumped by an Ar^+-ion laser, one AOM and one mechanical shutter. The two beams are overlapped on a beam splitter behind the cryostat.

7.2 Results

The constructed qubit can be seen in Figure 6.5 on page 38. After the construction we probed the qubit structure repeatedly. After about 6 probing scans the excitation laser was turned on and 6 more probing scans were carried out. After that the excitation laser was turned off and then 6 more probing scans were performed. The resulting signal can be seen in Figure 7.2.

In the figure one can clearly see that the background is increased when the excitation laser is switched on. This background is not considered to interfere with the measurements since it mostly is caused by reflections in the optical windows when the beam enters the cryostat.

The 18 recordings of the qubit were analysed by fitting a *Gaussian* line profile to them. A few examples are given in Figure 7.3.

The width and height of the qubit is plotted in Figure 7.4. In the figure different marks have been used for when the excitation laser was turned on and off. The first six marks (crosses) are measurements before the excitation laser was switched on, the following six (marked with rings) are when the laser was turned on and the last six (marked with crosses) are after the laser was switched off.

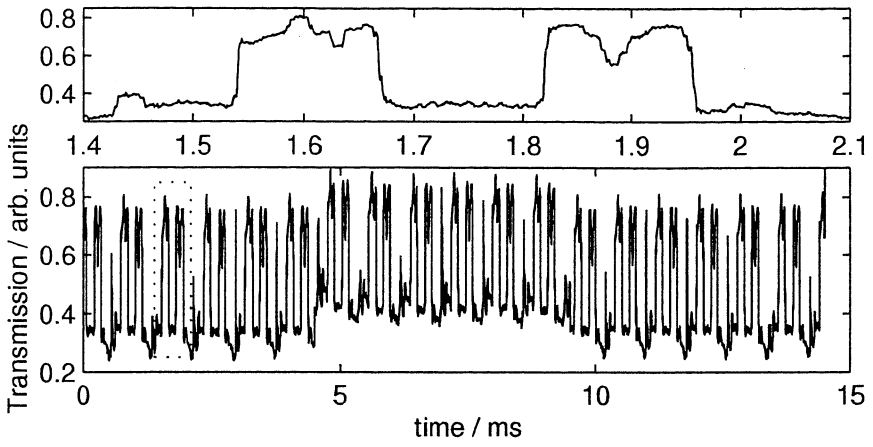

Figure 7.2: The picture shows the 18 consecutive probes of the qubit. It is very clear that the background increased when the excitation laser was turned on. The top image shows an enlargement of the dotted box in the lower picture.

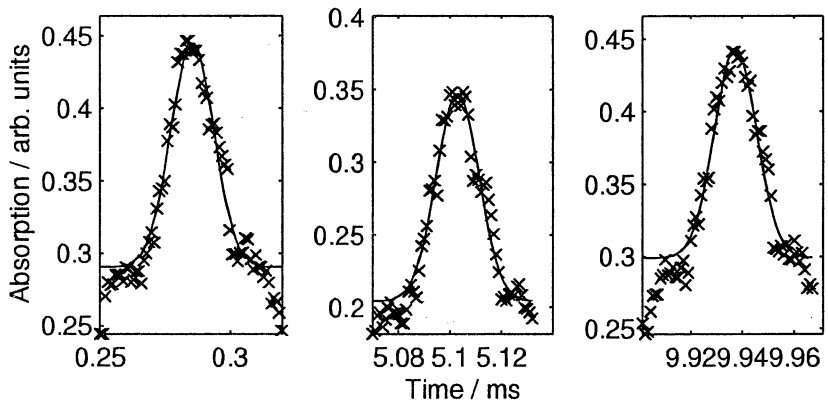

Figure 7.3: The pictures show *Gaussian* curves fitted to the experimental data, before the excitation laser is turned on (left), during (middle) and after it is turned off (right). The data has been transformed from a transmission to an absorption spectrum.

7.3 Discussion

In section 2.2 we discussed the theory concerning the excitation-induced frequency shifts. The shift of neighbouring ions was calculated. On the other hand we made no calculations regarding the broadening of spectral lines. This can be done according to the methods in [12]. If this is done we get a value of tens of kHz. To calculate this we have to estimate a value for the average distance to the nearest neighbour.

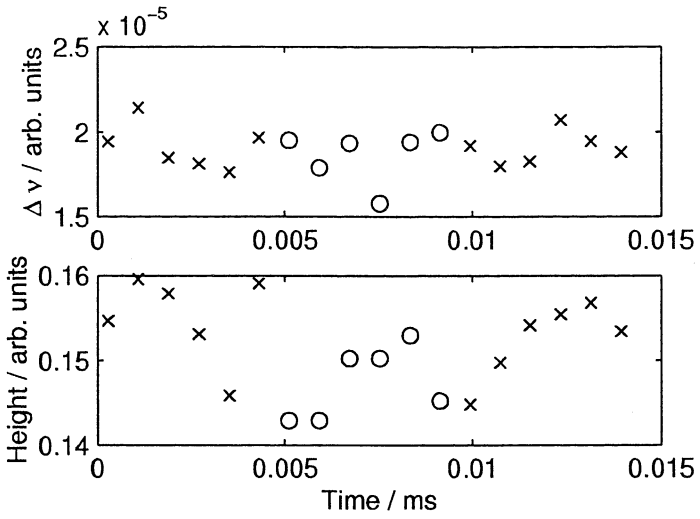

Figure 7.4: The width (top) and height (bottom) of the qubits. The width and height have been calculated by fitting *Gaussian* curves to the experimental data.

From the expected broadening of the qubit there does not come much hope of seeing the excitation induced frequency shift in this material. What we would expect to see is a broadening of the qubit and possibly a decrease in height.

The effects should gradually decrease when the laser is switched off since the excited ions are relaxed. The values should change according to the decay of the upper state population.

From the results shown in Figure 7.4 it is not clear if any effects are visible. Even if the recorded heights show some correlation to the expected behaviour it is not possible to make any statements. The main reason for this is that these recordings were made whith a larger background signal. The variations in the fitted data is also too large to make any conclusions about the excitation-induced effects.

The excitation induced frequency shift is expected to be larger if the Eu^{3+} ions are doped into $YAlO_3$. This is caused by a larger difference in upper and lower state permanent electric dipole moment and smaller average nearest neighbour distance. It may also possible to decrease the average nearest neighbour distance by using one of the satellite lines, see section 8.1 on page 44, and by using better detection techniques, see section 8.2 on page 44.

Chapter 8

Conclusions and outlook

The first step towards realising the quantum computer scheme proposed [13] has successfully been demonstrated as seen in Figure 6.5. This is very promising for the implementation of this quantum computing concept. But there are still a few things that have to be studied and a few that have to be improved.

Further studies of the ion-ion interaction have to be carried out. Without its verification the different qubits will have no way of controlling one another, as for instance in the controlled-NOT gate. If the interaction is too weak it might be possible to increase it by using the satellite lines, se section 8.1.

The hyperfine splitting structure must also be verified, i.e. are we using the correct model or should it be inverted. This can be done by constructing one qubit and then make a NOT operation on it. If the correct model of the hyperfine splitting has been used this will be possible. If the incorrect one has been used it will be impossible to shift all the ions to the other qubit state.

If many manipulations on qubits are to be carried out the laser stability must be increased. One way of doing this is to lock the laser frequency to an absorption line in, e.g., Iodine. This can be achieved by using *Doppler-free spectroscopy* in conjunction with the lasers own stabilising equipment.

There must also be a way of shifting the lasers frequency by about 1 GHz in order to construct the second qubit. It might of course be a possibility to place the two qubits rather close in frequency.

Although much improvement on the signal-to-noise ratio has been achieved it will not be good enough when the next step of the scheme is implemented. This is due to the fact that several of the ions from the qubit constructed in Figure 6.5 will be moved (to the reservoir state) when refining the state using the ion-ion interaction. One way of increasing the signal-to-noise ratio is illustrated in section 8.2. This technique will also deal with the problem of making the qubits experience top-hat intensity profiles spatially.

8.1 Increasing the ion-ion interaction

If the excitation induced frequency shifts are too small in the central part of the spectrum there is a possibility of using the satellite lines of the spectrum. The satellite lines consist of dopant ions that sit closer together in the crystal. This has been studied in $Eu^{3+} : YAlO_3$ by *Yamaguchi et al.* [27].

We have also observed such satellite lines in $Eu^{3+} : Y_2SiO_5$ in conjunction with our hole burning experiments, see Figure 8.1.

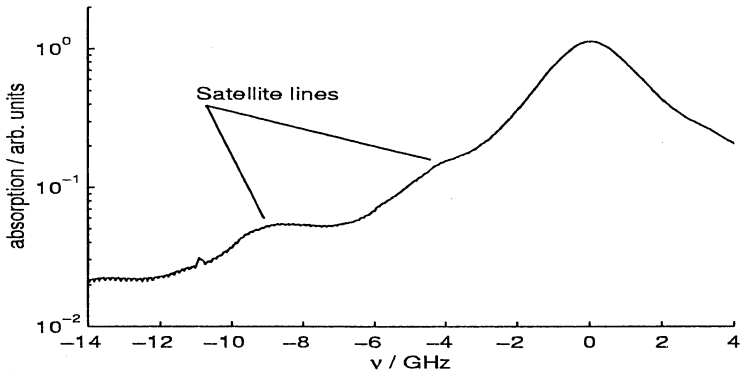

Figure 8.1: Satellite lines found in the spectrum of $Eu^{3+} : Y_2SiO_5$. The satellite lines are visible on the left slope of the absorption profile.

8.2 Top hat intensity profiles

One of the most important problems in the rare-earth-ion quantum computer scheme is to be able to make all the ions within the computer experience the same pulse area.

One way to establish the wide (spatial) holes around the $|1>$ and $|0>$ states is to use a larger beam in the initial optical pumping of the states. Then, in order to get the qubit started, a fairly small beam diameter should be used in order to only shift the middle ions back into the holes. The probing beam diameter should be somewhere in between. This gives top hat intensity profile for all the ions in the qubit.

Using three different beam diameters could be achieved with three different beam paths and overlapping them in front of the cryostat or by some sort of electronically controlled telescope.

One way of getting around this is by using a technique illustrated in [26]. The main idea is to image the focus inside the crystal at a pinhole after the cryostat. The image of the focus should be a lot larger than the diameter of the pinhole. The pinhole will only transmit the parts of the *Gaussian* beam where the spatial

intensity distribution is small. The technique is schematically illustrated in Figure 8.2.

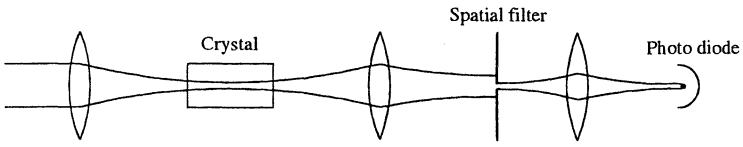

Figure 8.2: Illustration of how the principle of a pinhole at the detection side can be carried out.

In the experiment carried out by *Greiner et al.* in [26] they used a focus (in the crystal) with the diameter 140 μm. This was magnified ~ 2.5 times onto a 25 μm pinhole. The resulting difference in intensity on the different observed ions was around 1%. This is essentially a top-hat intensity distribution.

This would allow us to use one beam diameter throughout the whole experiment. By doing it this way the atoms in the sample will not experience the same pulse area, but we will only look at the ones that have the same pulse area.

Acknowledgements

First of all I would like to thank *Stefan Kröll* for giving me the opportunity to do my master's thesis at the atomic physics division, for his valuable help and for his encouragement.

I would like to thank the rest of the photon-echo group for their help and for our fruitful discussions, especially *Lars Levin* and *Mattias Nilsson* whom I have worked with during the last few months.

I would also like to thank *Åke Bergkvist* for his help with the electronic equipment.

At last I would like to thank my girlfriend, *Elisabeth Wieslander*, for all her love and support.

Bibliography

[1] David Deutsch, *Quantum Theory, the Church-Turing principal and the universal quantum computer*, Proc. Roy. Soc. Lond. **A 400**, 97-117 (1985).

[2] Andrew Steane, *Quantum Computing*, arXiv:quant-ph/9708022 v2, (1997).

[3] Dirk Bouwmeester, Artur Ekert and Anton Zeilinger, *The Physics of Quantum Information*, Springer-Verlag (2000).

[4] Colin P. Williams and Scott H. Clearwater, *Explorations in quantum computing*, Springer-Verlag TELOS (1997).

[5] C.H. Bennet, G. Brassard, C. Crépeau, R. Josza, A. Perez and W.K. Wootters, *Teleporting an unknown quantum state via dual classical and Einstein-Podolsky-Rosen channels*, Physical Review Letters **70**, 1895 (1993).

[6] A. Einstein, B. Podolsky and N. Rosen, *Can quantum-mechanical description of physical reality be considered complete?*, Physical Review **47**, 777 (1935).

[7] Andrew Steane, *Error correcting codes in quantum theory*, Physical Review Letters, **77**, 793 (1995).

[8] P.W. Shor, *Polynomial-time algorithms for prime factorization and discrete logarithms on a quantum computer*, Proc. 35th Anuual symp. on Foundations of Computer Science, Santa Fe (1994).

[9] Robert W. Boyd, *Nonlinear Optics*, Academic Press (1992).

[10] Cecilia Nilsson, *Femtosecond optical bit multiplication by photon echoes excited with spectrally modulated laser pulses*, Master's thesis, LRAP-213, (1996).

[11] L. Allen and J.H. Eberly, *Optical resonance and two-level atoms*, John Wiley & Sons (1975).

[12] Felix R. Graf, Alois Renn, Gert Zumofen and Urs P. Wild, *Photon-echo attenuation by dynamical processes in rare-earth-ion-doped crystals*, Physical Review B **58**, 5462 (1998).

[13] Nicklas Ohlsson, R. Krishna Mohan and Stefan Kröll, *Quantum Computer Hardware based on Rare-earth-ion doped Inorganic Crystals*, submitted to Physical Review Letters, (2000).

[14] Orazio Svelto, *Principles of Lasers, 4^{th} ed.*, Plenum, page 335 (1998).

[15] Coherent. *699 Ring dye laser instruction manual.*

[16] H. Hertz, L-Å. Nilsson. *Konstruktion och testning av digital våglängdsmeter*, Master Thesis's, Lund Institute of Technology (1980).

[17] Eugene Hecht, *Optics, 3^{rd} ed*, Addison-Wesley (1998).

[18] Martin J. Buerger, *Elementary crystallography*, Wiley, 126 (1963).

[19] B.A. Maksimov, Y.A. Kharitonov, V.V. Illyukin and N.B. Belov, Soviet Physics Crystallography **15**, 806 (1971).

[20] Ryuzi Yano, Masaharu Mitsunaga and Naoshi Uesugi. *Ultralong optical dephasing time in $Eu^{3+} : Y_2SiO_5$.* Optics Letters **16**, 1884 (1991).

[21] Ryuzi Yano, Masaharu Mitsunaga and Naoshi Uesugi. *Nonlinear laser spectroscopy of $Eu^{3+} : Y_2SiO_5$ and its application to time-domain optical memory.* J. Opt. Soc. Am. B **9**, 992 (1992).

[22] *Handbook of Chemistry and Physics, 74^{th} ed.*, **6:149**, CRC Press (1992).

[23] Mattias Nilsson. *Multi-bit data storage using photon echoes*, Master's thesis, LRAP-263, Lund Institute of Technology, section **3.4**, (2000).

[24] Tektronix, *TDS 520A, 524A, 540A, & 544A User Manual* (1993).

[25] Keith Holliday, Mauro Croci, Eric Vauthey and Urs P. Wild, *Spectral hole burning and holography in an $Y_2SiO_5 : Pr^{3+}$ crystal*, Physical Review B **47**, 14741 (1993).

[26] C. Greiner, B. Boggs, T. Loftus, T.Wang and T. W. Mossberg, *Polarization-dependent Rabi frequency beats in the coherent response of Tm^{3+} in YAG*, Physical Review A **60**, R2657 (1999).

[27] M. Yamaguchi, K. Koyama and T. Suemoto, *Perturbed ion sites in $Eu^{3+} : YAlO_3$ studied by optical-rf double-resonance spectroscopy.* Physical Review B **59**, 9126 (1999).

Appendix A

Theoretical spectrum of $Eu^{3+} : Y_2SiO_5$

When doing hole burning experiments there will be a lot of extra peaks all over the spectrum as seen in Figure 5.2 on page 32. The spectral location for these holes and anti holes can be calculated from the information given in table 3.1 on page 22.

Below I will use the labels from the quantum-computing scheme on page 15 on the three ground state hfs-levels. The three excited hyperfine states are called $|e_2>$, $|e_1>$ and $|e_0>$, se Figure A.1.

If we begin by looking at what happens to those atoms that are in the state $|a>$ at the burning frequency ν_0. The atoms in state $|1>$ and $|0>$ can be treated in a similar way.

There are three types of $|a>$ atoms that are absorbing at any given frequency, ν_0. Those who have absorption at the $|a> \rightarrow |e_2>$, $|a> \rightarrow |e_1>$ and $|a> \rightarrow |e_0>$ transitions, se Figure A.1.

When the optical pumping stops all the atoms that were originally in state $|a>$ will have been moved to states $|1>$ and $|0>$. If we at this point look at the spectrum we will have nine transitions with low absorption, all the transitions from the $|a>$ state. Their absorption is decreased by a factor of 1/9. Three of these have the same frequency, ν_0, and this will lead to a hole who's absorption is reduced by one third. When transitions from the two other ground states are taken into account this hole at ν_0 will have zero absorption as expected.

The six remaining transitions from $|a>$ will give rise to side-holes at $\nu_0 + \nu_1$, $\nu_0 + \nu_2$, $\nu_0 + \nu_1 + \nu_2$, $\nu_0 - \nu_1$, $\nu_0 - \nu_2$ and $\nu_0 - \nu_1 - \nu_2$. The depth of these holes will increase three times when transitions from $|1>$ and $|0>$ are taken into account. The final depth will thus be one third.

After the optical pumping all the original $|a>$ atoms will be evenly distributed over the $|1>$ and $|0>$ states. This will give rise to anti holes in the spectrum. If

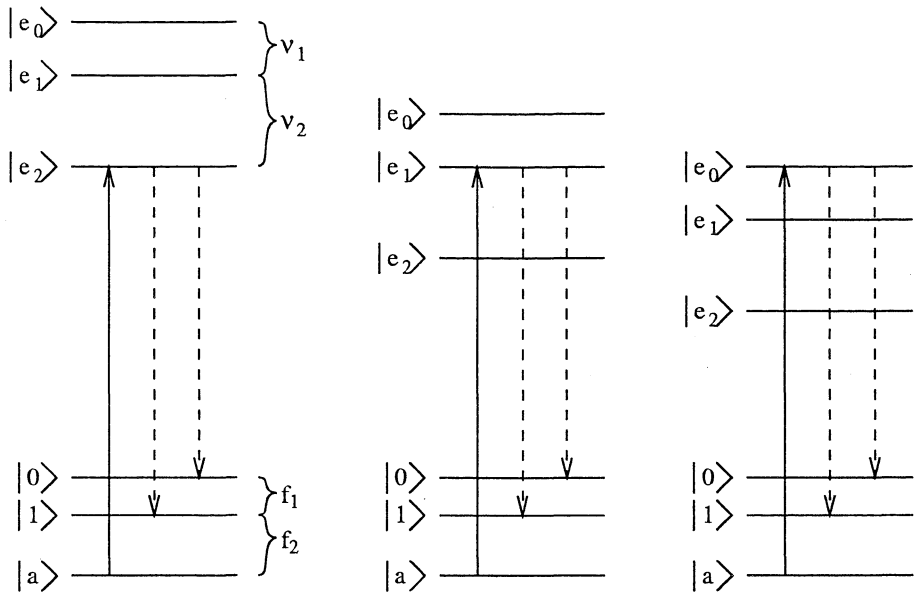

Figure A.1: Energy diagram of transitions at ν_0 from the $|a>$ state.

one look at the $|1>$ state in the left picture in Figure A.1 we see that this will give 3 anti holes located at frequencies $\nu_0 - f_2$, $\nu_0 - f_2 + \nu_2$ and $\nu_0 - f_2 + \nu_1 + \nu_2$. The height of these anti-holes are $1/18$ and there are $3 \cdot 18 = 56$ of them.

One also has to take both the isotopes into account. This leads to 6 more side holes and 56 more anti holes. The depth of the side holes decreases to $1/6$ and the height of the anti holes decreases to $1/36$. The burnt hole at ν_0 will of course still have zero absorption.

A.1 M-file for generation of theoretical spectrum

The following *MATLAB* M-file will calculate the theoretical spectra of Eu^{3+} : Y_2SiO_5 used in Figure 5.2 on page 32.

```
ga = [0 29.5 57.3]*1e6; % ground level isotope 1
gb = [0 76 148]*1e6;  % ground level isotope 2
ea = [0 63 108]*1e6; % excited level isotope 1
eb = [0 160 274]*1e6;  % excited level isotope 2

fmin = -0.75e9; % min frequency
fmax = 0.75e9;  % max frequency
fstep = 0.1E6;  % frequency step
f = [fmin:fstep:fmax]; % frequency vector
ampl = ones(size(f));  % original amplitude
df = 3E6;  % halfwidth of the peak.
```

```
% --- sideholes ---
fsa = [ea -ea 0 ea(2)+ea(3) -ea(2)-ea(3)];
fsb = [eb -eb 0 eb(2)+eb(3) -eb(2)-eb(3)];
for f0 = [fsa fsb],
   ampl = ampl - lineshape(f, f0, df)/6;
end
% --- xxxxxxx ---

% --- anti holes ---
fa = [fsa-ga(2) fsa-ga(3) fsa-ga(2)-ga(3), ...
      fsa+ga(2) fsa+ga(3) fsa+ga(2)+ga(3), ...
      fsb-gb(2) fsb-gb(3) fsb-gb(2)-gb(3), ...
      fsb+gb(2) fsb+gb(3) fsb+gb(2)+gb(3)];
for f0 = fa,
   ampl = ampl + lineshape(f, f0, df)/36;
end
% --- xxxxxxx ---


% discard unuseful data
fteo = f;
dteo = ampl;
p = find(abs(dteo-1)<0.00005);
dteo(p) = [];
fteo(p) = [];
```

This m-file also uses the function *linehsape.m* shown below.

```
function [line] = lineshape(f,f0,df)
line = exp(-4*log(2)*((f-f0)./df).^2);
```

Appendix B

Pulse generation for qubit construction

The figures below are an illustration of how the pulses in the qubit construction experiment looked like and how they were created.

In Figure B.1 we can see what the pulse train looked like. The S_S and S_D are the mechanical shutters controlling the single AOM beam and both beams into the cryostat respectively (compare with Figure 6.1).

AOM_D is the double AOM set-up, the two AOMs are controlled by the same control unit. This fact and their geometrical placement are the reasons why they do not give any beam deviation.

The V_T is the signal that controls the frequency shift of the AOM and MOD is the on-off signal.

The last line is the EOM, which gives low transmittance when the signal goes high.

The pulse train starts with, T_{01}, which opens the two mechanical shutters. Since these are a bit slow we wait for about 50 ms before the first burning sequence is started. At time A_1 the burning around $|0>$, $|1>$ and at $|a>$ starts. The frequency to the double AOM system is continuously scanned and they are opened at times corresponding to frequencies of the $|0>$ and $|1>$ states. In order to simplify the electronic set-up the single AOM were opened at the same times.

At time B_1 the first burning sequence is finished. The mechanical shutter controlling the beam directed at $|a>$ is closed. About 50 ms later the probing sequence is started, the EOM is turned on decreasing the power going through the double AOM by a factor of 50. The frequency of the double AOM is scanned over the maximum range and it is opened for about 80 μs.

After the probing sequence, the first *DG535* triggers the second one. Time T_{02}

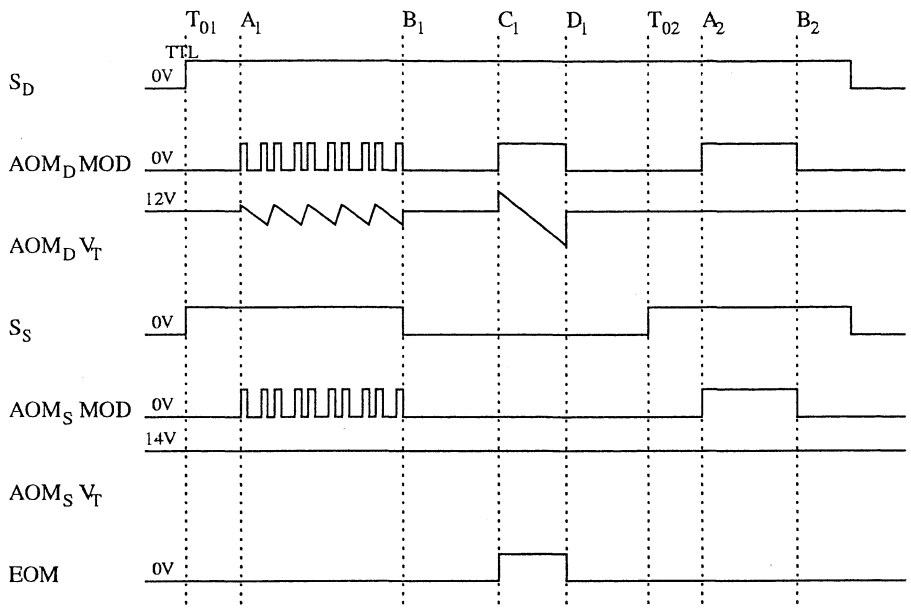

Figure B.1: Pulse sequences for qubit construction. The voltages given at different times to different components are shown on the horizontal lines. The AOM_i MOD signal opens the acousto-optic modulators when given a TTL input and the V_T controlls the frequency shifts of the AOMs. The mechanical shutters, S_D and S_S, are opened when the signal goes high and the electro-optic modulator decreases the laser lights power when it goes high.

opens the closed mechanical shutter. Between A_2 and B_2 the burning at $|1>$ and $|a>$ are performed.

Typical times in this pulse train are:

T_{01} - A_1	50 ms
A_1 - B_1	600 ms
B_1 - C_1	50 ms
C_1 - D_1	80 μs
T_{02} - A_2	50 ms
A_2 - B_2	300 ms

Table B.1: Approximate time durations for the pulses in the qubit construction experiment.

To make measurements on the prepared qubit the above sequence is used with different times. The times $A_1 - B_1$ and $A_2 - B_2$ are set to zero. This will give the signals necessary to make the probing beam.

In order to achieve the pulse trains above the electronic equipment were configured in the way described by Figure B.2 below.

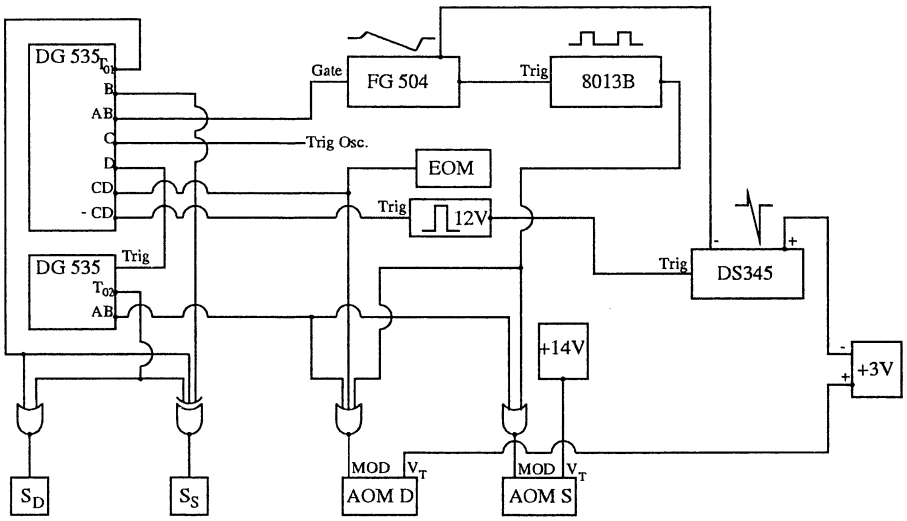

Figure B.2: Configuration of electronic equipment used in the qubit construction. A wide variety of pulse and waveform generators are used. In addition to this a few logic gates are used, three *or*-gates (the output high when any input is high) and one *xor* (the output is high if an odd number of inputs are high).